MSc. Advanced Computational Methods for Aeronautics, Flow Management and Fluid Structure Interaction. Imperial College of London, Year 2006/2007

# Control of Hairpins vortices using body forces

JULIEN HOESSLER

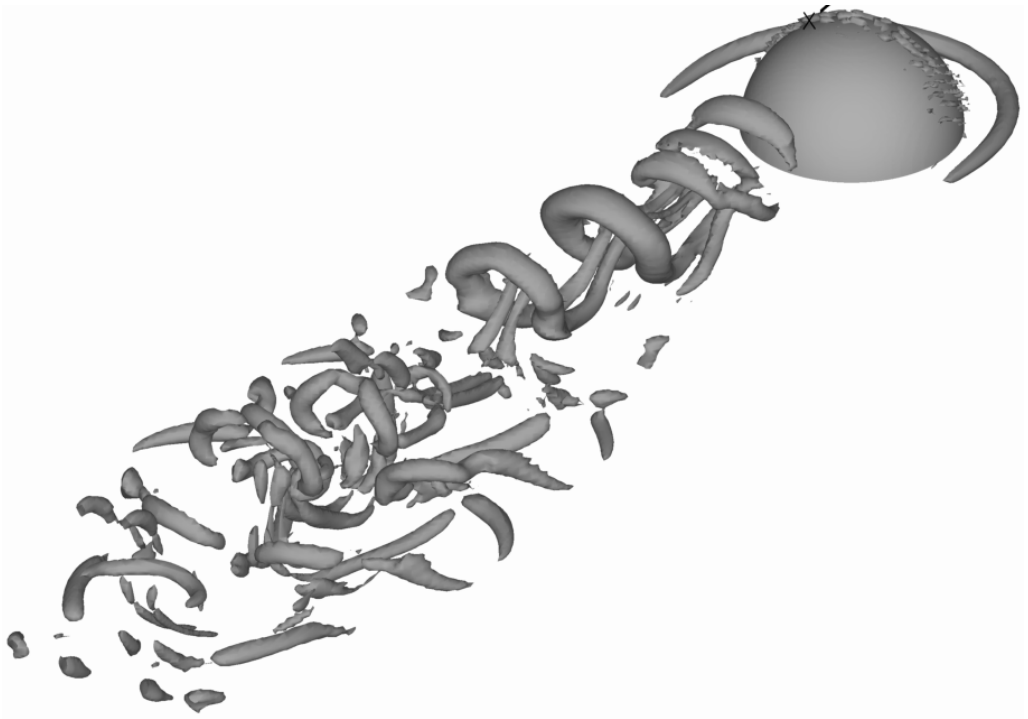

I have neither given nor received assistance except where acknowledged
September 21, 2007

# Contents

# Acknowledgements

I would like to thank my two supervisors Dr. Lardeau and Dr. Rossi for proposing me such an interesting project subject, their disponibility and all the things I have learnt working with them, except improving my english level. I'd also like to thank all my MSc colleagues for this great year we spent.

# Notations

## General variables

| | |
|---|---|
| $x = x_1$ | Downstream direction |
| $y = x_2$ | Transverse direction |
| $z = x_3$ | Cross direction |
| $u_i$ | Velocity component along the direction $i = 1 \dots 3$ |
| $\mathbf{u}$ | Velocity vector |
| $a_i$ | Lagrangian acceleration component along the direction $i = 1 \dots 3$ |
| $\mathbf{a}$ | Lagrangian acceleration vector |
| $p_m$ | Modified pressure field |
| $p_i$ | Modified pressure field gradient along the direction $i = 1 \dots 3$ |
| $L_x$ | Domain size along the direction $x$ |
| $L_y$ | Domain size along the direction $y$ |
| $L_z$ | Domain size along the direction $z$ |
| $n_x$ | Number of nodes along the direction $x$ |
| $n_y$ | Number of nodes along the direction $y$ |
| $L_z$ | Number of nodes along the direction $z$ |
| $\Delta_x$ | Spatial step along the direction $x$ |
| $\Delta_y$ | Spatial step along the direction $y$ |
| $\Delta_z$ | Spatial step along the direction $z$ |

## Mean and RMS related variables

| | |
|---|---|
| $U_i$ | Mean velocity component along the direction $i = 1 \dots 3$ |
| $\overline{u_i}$ | RMS velocity component along the direction $i = 1 \dots 3$ |
| $\overline{u_i u_j}$ | Reynolds tensor components |
| $k$ | Turbulent Kinetic Energy |

## Hairpin flow related parameters

| | |
|---|---|
| $R$ | Radius of the hemisphere |
| $\delta_{99}$ | Thickness of the incoming boundary-layer |
| $\delta$ | Displacement thickness of the boundary-layer |
| $\theta$ | Momentum thickness of the boundary-layer |
| $H = \frac{\delta_{99}}{R}$ | Height ratio between the boundary-layer thickness and the hemisphere radius |
| $U_\infty$ | velocity of the inlet above the boundary layer |
| $U_\tau$ | velocity that would occur at the top of the hemisphere if the boundary layer was not perturbated |
| $Re_\infty = \frac{U_\infty R}{\nu}$ | Reynolds number defined using $U_\infty$ |
| $Re_\tau = \frac{U_\tau R}{\nu}$ | Reynolds number defined using $U_\tau$ |

| | |
|---|---|
| $Q$ | Q-criterion value |
| $f$ | Frequency associated to the hairpins shedding |
| $St = \frac{fR}{U_\infty}$ | Strouhal number associated to the hairpins shedding |

# Chapter 1

# Introduction

With fuel prices increasing greatly and the growing concern over global warming, the aeronautics industry is required to reduce the fuel consumption and pollution levels drastically within ten years. If an important part of these reductions can be achieved by improving the engines and managing better the global traffic, it wil not be enough. Thus the drag reduction may be one of the remaining steps to reach these quality criterions, and is expected to contribute to ten to twenty percents of the flight consumption reduction.

The aim of this study is to find a way to control hairpin structures using plasma forcing, as they are supposed to contribute strongly to the friction term applied to the wall on a turbulent boundary layer. Plasma actuators are a good candidate to control that kind of structures as they present the great advantage of being non-intrusive. Moreover, some experiments have already been performed, for instance by [15], showing its efficiency to delay the stall on wings. Here, the aim is not to change the physics of the flow, but rather to find a way to control a certain kind of structures to reduce their drag contribution on a wall. Controlling them means driving them away from the surface or reorganising them to make their ability to exert forces on the surface reduced. In order to do so, their physics must be studied, which will be one of the objectives of the present study. In a general turbulent boundary layer, hairpins are mixed and interacting with lots of other coherent structures ([17]), and thus, in order to focus on them, simulations will be performed to generate a flow where hairpins are easily identified, and as periodical and unperturbated by secondary turbulent structures as possible.

The flow considered here is the flow around an hemisphere fixed on a flat plate. The incoming velocity profile is a laminar boundary-layer Blasius profile. The velocity above the boundary layer is $U_\infty$. The hemisphere then perturbates this laminar incoming flow to create a stable and strongly periodical street of hairpins, at least for some boundary-layer height ratios $H$ and Reynolds numbers $Re$ which are the two major parameters. The height ratio $H$ between the boundary-layer thickness $\delta_{99}$ and the hemisphere radius $R$, indicates the level of perturbation of the boundary-layer by the hemisphere, as illustrated in figure 1.1

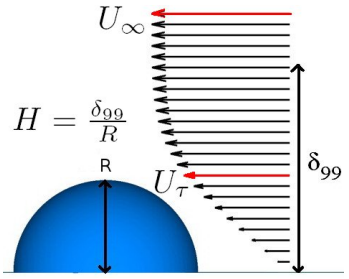


Figure 1.1: Definition of the Height ratio $H$

This rather simple flow has been designed and studied experimentaly by [1]. They argue that the hairpin vortices play a key role in the developpement and sustaining of the turbulent process in the near wall region of a turbulent boundary-layer. Their objectives were to determinate the shedding conditions and detached characteristics as well as the formation and evolution of hairpin vortices, examine the secondary structures generated and establish flow visualisations of the hairpins and these secondary structures. It will provide experimental data, yet more qualitative than quantitative for the present study. The shedding and the evolution of hairpin are also investigated in this study, as well as more numerical related parameters like the effect of bockage and domain length. And once these parameters and their effects are studied to define the best case for control in terms of hairpin quality and numerical efficiency, the plasma actuators are introduced.

A Reynolds number $Re_\tau$ above $1000$ would cost too much calculation time[1] and this value is sufficient for control purposes. The Reynolds number investigated are thus between $100$ and $1000$, covering the transition from steady to unsteady flow spotted at $Re = 120$ by [1] and the full regime above this value. The second parameter is the height ratio. The lower this number is, the more the hairpins are perturbated, as the obstacle covers more and more of the high strain zone of the incoming boundary-layer. It will be seen that $H = 2$ provides a proper flow. A comparative case will be performed at lower $H$ ratio to show how the periodicity of the hairpin shedding is degenerated, and lead to more secondary structures. Figure 1.2 represents the domain that will be used as well as the boundary conditions applied, which will be detailed in the first chapter.

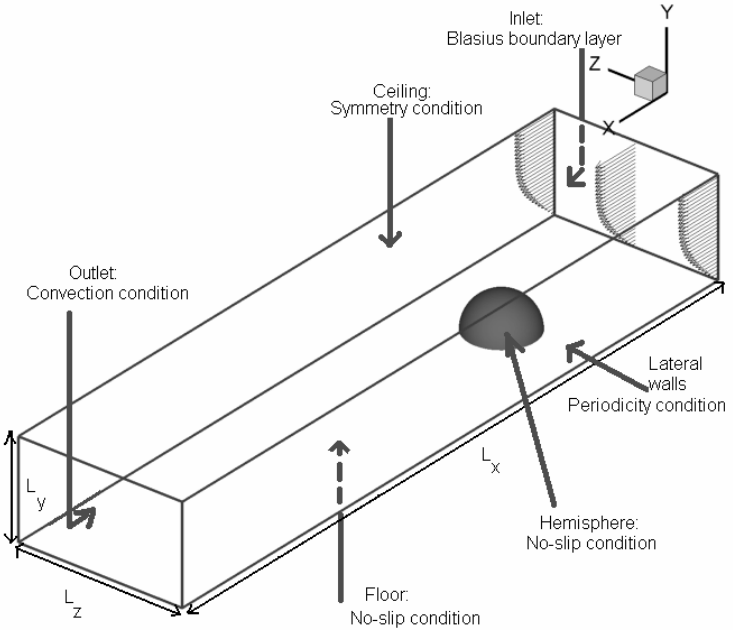


Figure 1.2: Sketch of the domain considered as well as its associated lengths and boundary conditions applied

Some alternative ways have ben used to generate simple hairpin vortices: [20] use a mixing plane, and [8] use fluid injection techniques.

Few numerical simulations using this framework have been performed. [9] had quite different objectives from the one for the present study. However, some visualisations of the hairpin vortices, as well as the shedding Strouhal numbers $St$ will be compared. Far more simulations have been performed for the slightly simular study of the flow past a sphere, and can be found, for instance, in [10], [13] or [4]. These results are briefly described here to present the type of numerical simulations realised as well as the mesh and the

[1] all the simulations are run on a workstation

blockage ratio used. If the situation is not exactly similar, both the sphere and hemisphere can shed hairpins around the same Reynolds number, and thus the study of these case is an efficient way to reduce the number of simulations necessary create a proper mesh.

# Chapter 2

# Numerical methods

Direct Numerical Simulations (DNS) are performed using the pseudo-spectral code *Incompact3d* ([12] and [11]). The incompressible non-dimensionalised Navier Stokes equations are considered:

$$\frac{\partial \mathbf{u}}{\partial t} = -\frac{1}{\rho}\nabla p_m - \omega \times \mathbf{u} + \nu \nabla^2 \mathbf{u} \tag{2.1}$$

$$\nabla.\mathbf{u} = 0 \tag{2.2}$$

where $\nu$ is the constant kinematic viscosity, $\rho$ the constant density, $p_m$ the modified pressure field, $\mathbf{u}$ and $\omega$ being the velocity and vorticity fields. The modified pressure field is related to the pressure field by:

$$p_m = p + \frac{\rho}{2}\mathbf{u}.\mathbf{u} \tag{2.3}$$

Equations (2.1, 2.2) are directly solved on a cartesian grid. Sixth-order compact centered difference schemes are used to evaluate all the spatial derivatives. Time integration is performed with a third-order low-storage Runge-Kutta method.

The incompressibility condition is ensured via a fractional step method introducing a Poisson equation for the pressure. This equation is directly solved in the framework of the modified spectral formalism, using $3D$ Fast Fourier Transforms (FFT3D). The solver has been modified to process not only periodic/free slip boundary conditions, but also Dirichlet conditions for velocity coupled with homogeneous Neumman conditions for pressure. It allows the introduction of a grid stretching in one direction. [11] can be consulted for a more detailed description of this solver.

## 2.1 Flow configuration

### 2.1.1 Domain dimensions

The dimensions chosen for the different cases performed can be found on table 2.1. The mesh is cartesian. The idea of a Direct Numerical Simulation (DNS) is to solve all the turbulent scales. The only fixed dimension is $L_y = 10$. The influence of the two others will be investigated in chapter 4. The length $L_z$ will be set to 5 and 10 to investigate the effect of the blockage ratio, while the length $L_x$ will be set to 20 and 30 to investigate the effect of the outlet condition on the flow.

As far as $H$ is concerned, three ratios are performed for a fixed Reynolds number $Re_\tau$ in order to investigate the effect of this parameter.

| | Case name | $L_x$ | $L_y$ | $L_z$ | $n_x$ | $n_y$ | $n_z$ | $ncl_x$ | $ncl_y$ | $ncl_z$ | $Re_\tau$ | $H$ |
|---|---|---|---|---|---|---|---|---|---|---|---|---|
| 1 | $20 \times 10 \times 5$ | 20 | 10 | 5 | 361 | 121 | 90 | 2 | 2 | 0 | 1000 | 2 |
| 2 | $20 \times 10 \times 10$ | 20 | 10 | 10 | 361 | 121 | 180 | 2 | 2 | 0 | 1000 | 2 |
| 3 | $30 \times 10 \times 5$ | 30 | 10 | 5 | 541 | 121 | 90 | 2 | 2 | 0 | 1000 | 2 |
| 4 | $20 \times 10 \times 5 - H = 1.5$ | 20 | 10 | 5 | 361 | 121 | 90 | 2 | 2 | 0 | 1000 | 1.5 |
| 5 | $20 \times 10 \times 5 - H = 1$ | 20 | 10 | 5 | 361 | 121 | 90 | 2 | 2 | 0 | 1000 | 1 |
| 6 | $20 \times 10 \times 5 - 750$ | 20 | 10 | 5 | 361 | 121 | 90 | 2 | 2 | 0 | 750 | 2 |
| 7 | $20 \times 10 \times 5 - 500$ | 20 | 10 | 5 | 361 | 121 | 90 | 2 | 2 | 0 | 500 | 2 |
| 8 | Inlet-validation | 10 | 10 | 0.2 | 181 | 121 | 4 | 2 | 2 | 0 | 1000 | 2 |
| 9 | 2D-actuator | 10 | 10 | 0.2 | 181 | 121 | 4 | 2 | 2 | 0 | 1000 | 2 |
| 10 | Blasius forcing | 10 | 10 | 0.2 | 181 | 121 | 4 | 2 | 2 | 0 | 1000 | 2 |
| 11 | 3D-actuator | 8 | 10 | 5 | 145 | 121 | 90 | 2 | 2 | 0 | 1000 | 2 |
| 12 | Hairpin forcing | 8 | 10 | 5 | 145 | 121 | 90 | 2 | 2 | 0 | 1000 | 2 |

Table 2.1: Table of the simulations performed and their associated parameters

### 2.1.2 Mesh resolution

The table 2.1 provides the resolutions $n_x$, $n_y$ and $n_z$ along the three directions of the mesh. In order to avoid dealing with the effects of mesh modifications in the calculations, all the simulations, whatever the value of the Reynolds number is, are performed on the most refined mesh defined for $Re_\tau = 1000$. Using an height ratio $H = 2$ leads to a Reynolds number $Re_\infty = 1348$ according to Blasius tables given in [18].

The principle of Direct Numerical Simulation is to solve all the scales. As the flow is initially laminar, this does not provide a minimal cell size for the mesh. However, the laminar boundary layer will be correctly described if the first layer of nodes is located around $y^+ = 1$, $y^+$ being the non-dimensionalised distance to the wall. A refinement is used at the bottom, along the $y$ direction. Above $y = 2H$, the flow is only convected and is only meshed to avoid a too strong blockage. Thus a coarse mesh in this area should not affect the physics of the flow. The mesh is set to get a $y^+ \leq 1$ all over the sphere, using the length obtained in the floor for the boundary layer. As this latter is supposed to thicken downstream, the most critical resolution is obtained right at the entrance of the domain for which the profile is completely characterized by the inlet velocity. In order to find the minimal spatial step $\Delta_y$, one has to solve the Blasius boundary-layer equation:

The Blasius boundary-layer is solution of the similarity problem defined by the following equation

$$ff'' + 2f''' = 0 \qquad \text{with} \qquad u_1 = U_\infty f'(\eta) \qquad \text{and} \qquad \eta = y\sqrt{\frac{U_\infty}{\nu x}} \tag{2.4}$$

If the height ratio is set to $H = 2$, the associated distance x corresponding to the length of development of the boundary-layer from the leading edge is defined by:

$$x = \left(\frac{H}{4.916}\right)^2 \frac{U}{\nu} \qquad \text{with} \qquad \nu = (Re_\infty)^{-1} \qquad \text{and} \qquad U = 1 \Rightarrow x = 215.67 \tag{2.5}$$

Then, using $x$, the wall shear stress can be defined:

$$\tau_w = \mu \left(\frac{\partial u_1}{\partial y}\right)_{y=0} = \alpha \mu U \sqrt{\frac{U}{\nu x}} = 6.16 \times 10^{-4} \qquad \text{with} \qquad \alpha = 0.33206 \tag{2.6}$$

$\alpha$ is a numerical constant appearing when solving the Blasius equations. As $\rho$ is set to 1, $\mu = \nu$. Then, knowing $\tau_w$, the reduced velocity $u_\tau$ can be defined at the wall:

$$u_\tau = \sqrt{\frac{\tau_w}{\rho}} = 2.48 \times 10^{-2} \tag{2.7}$$

$$y^+ = 1 \Rightarrow y_{min} = \frac{\nu}{u_\tau} = 2.99 \times 10^{-2}$$

Thus, the height of the first cell on the top of the sphere will be around $3 \times 10^{-2}$ along the $y$ direction. The number of point is set to 121 points for $L_y = 10$ (cf. figure 1.2)with a growth parameter of 1 (the definition of this growth parameter can be found in [11]). It leads to $\Delta_{y_{min}} = 2.4 \times 10^{-2}$ at the wall and $\Delta_y = 3.05 \times 10^{-2}$ at the top of the hemisphere. In the other two directions, the step is set to $\Delta_x = \Delta_z = 5 \times 10^{-2}$. This way, the aspect ratio is kept reasonneably low (below 2) and it reduces the number of elements $n_x$ and $n_z$. Because of the spectral resolution method used for the pressure, and the strong decrease in FFT efficiency when the points are not equally spaced, it is not worthwhile to use a refinement in more than a direction. So the mesh is uniform along $x$ and $z$, respectively the stream and cross-stream directions.
An a-posteriori validation of the mesh $y^+$ on the floor can be found in figure 2.1. Figure 2.1 shows that

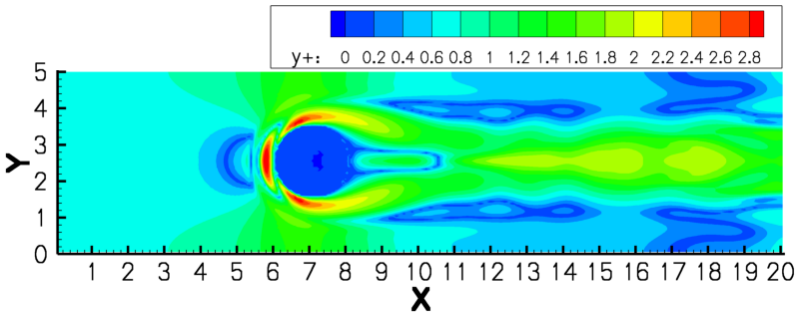


Figure 2.1: unsteady visualisation of the $y^+$ on the floor for the $20 \times 10 \times 5$ simulation

even though the value is not below 1 everywhere, it is below 2 behind the sphere. Only on the standing vortex region does $y^+$ reach 3, but in this region, the flow is still laminar and the increase is generated by the compression imposed by this standing vortex. The resolution specified above will thus be kept for all the other simulations.

## 2.2 Implementation and use of the Immersed Boundary Methods

In order to consider flows in presence of complex geometries, like an hemisphere in our case, the Immersed Boundary Method is used. It has the great advantage of being appliable on a cartesian grid, and thus avoiding the losses of accuracy and increases of computational costs that occur when using complex non-structured grids. A rather exhaustive description of the different Immersed Boundary Methods can be found in [7]. For the present code, a forcing method is considered. It consists in the imposition of a target velocity $\mathbf{u_0}(\mathbf{x}, t)$ on the velocity field $\mathbf{u}(\mathbf{x}, t)$ in the region of the obstacle. The objective is to verify the boundary condition at the walls of the obstacle. A direct method is used to evaluate the forcing term during the three sub-steps of the Runge-Kutta time advancement. A more detailed description of the implementation and the problem encountered for a moving object can be found in [11] and [5]. In the following, only the implementation of the target field evaluation will be considered.

Two different implementations are used. However, due to lack of time, the comparaison between these two methods is not performed for all the configurations, and the first method (zero velocity inside the obstacle) has been used in most of the simulations. However, sveral tests on the code have shown that if the mesh is resolved enough, and for a fixed obstacle, the results provided by the two methods are strongly similar.

### 2.2.1 Zero-velocity inside the hemisphere

The first and simpliest way to implement the Immersed Boundary Method is to force the velocity equal to zero for all the points inside the obstacle external surface which is defined in the case of a sphere by:

$$(x - c_1)^2 + (y - c_2)^2 + (z - c_3)^2 = R \tag{2.8}$$

where $C = (c_1, c_2, c_3)$ is the location of the hemisphere center. The process is strongly facilitated by the fact that the equation 2.8 is really simple and that the normals can also be easily obtained.
The forcing is applied at every substep of the iteration. The velocity field obtained thus contains a zero velocity inside the obstacle, and approximately zero on the surface. The only downsize of this method, which is really simple and fast, is that it does not lead to a velocity of exactly zero at the surface. The velocity field is forced at zero inside, but not all the points are at equal distance from the surface, which mean that the zero velocity is more or less at the surface depending on the proximity of the first inside and outside points, leading to a slightly deformed obstacle if this latter is defined as the zone of zero velocity. An illustration of it can be found in figure 2.2 which shows the hemisphere superposed with the cartesian mesh in a slice plance. A way to cope with this problem is to use the Mirror Flow technique.

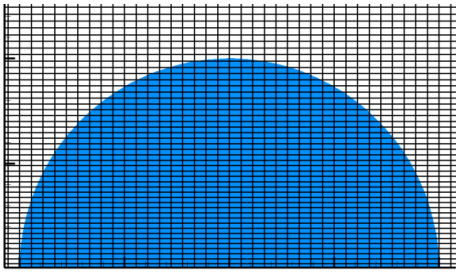

Figure 2.2: Superposition of the cartesian mesh with the hemisphere

### 2.2.2 Mirror flow inside the hemisphere

In the Mirror flow approach, every internal point of the mesh has its distance to the surface evaluated. Then its mirror relative to this surface is located. It usually does not correspond with a node of the mesh, so the velocity vector is evaluated by bilinear interpolation of the neighbouring nodes. Then, the velocity at the associated inner point is set to the opposite of the velocity vector obtained. This way, the velocity has to change of sign when crossing the obstacle surface, and the zero should be located on it, or at least closer than using the simple zero-inside approach. The figure 2.3 shows a simple example of this method in 2 dimensions

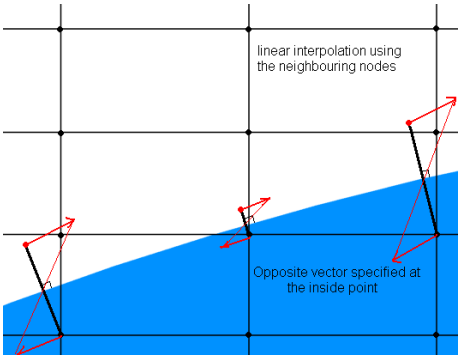


Figure 2.3: Mirror flow technique illustration in 2 dimensions

## 2.3 Boundary conditions

Figure 1.2 shows the considered domain. The table 2.1 contains the boundary condition parameters for the three directions $ncl_x$, $ncl_y$ and $ncl_z$. $ncl = 2$ means that a Dirichlet condition is applied along the direction, $ncl = 1$ is a Neumman condition, and $ncl = 0$ is a periodic condition.

- On the lateral faces, periodic conditions are applied, and thus $ncl_z = 2$ in all the cases.
- In the $y$ direction, the velocities are prescribed, and thus $ncl_y = 2$.
  - A no-slip condition is applied on the floor
  - A free-slip condition is applied on the ceiling, meaning that the only non-zero component of the velocity field is $u_1$. It is considered that the ceiling is far enough from the obstacle to get a convected flow along the direction $x$ with $u_1 = U_\infty$
- On the $x$ direction, the velocities are also prescribed, and $ncl_x = 2$.
  - The outflow boundary condition at $x = L_x$ is deduced by solving a simplified convective equation for the velocity components at the last nodes:

$$\frac{\partial \mathbf{u}}{\partial t} + U_\infty \frac{\partial \mathbf{u}}{\partial x} = \underline{0} \tag{2.9}$$

  - At the inlet, the Blasius equation 2.4 is solved using a second-order Runge-Kutta method in the code[1] to provide $u_1(y)$ at $x = 0$. Both $u_2$ and $u_3$ are set to zero, and there is no noise added unless precised otherwise.

### 2.3.1 Recycled inlet condition

For the domains used for the forcing cases, they are provided with an inlet condition extracted from a $iso - X = 12$ ($217^{th}$ point along the x direction) plane of the $20 \times 10 \times 5$ simulation, as used by [12]. Using the hypothesis of frozen turbulence, getting this plane at every time-step and introducing as an inlet of a new simulation is equivalent to a complete resolution of the flow downstream while reducing strongly the iteration time. But on top of this, the flow is considered as periodical enough to loop this condition over the shedding period in order to create an hairpin alley. The principle of this method is to find an $iso - X$ plane for which the flow is periodical. We start recording this plane at each time-step at $t = t_0 = n_0 \Delta_t$, and if after $n_1$ time-steps, which corresponds to a shedding period, the plane for $t = (n_0 + n_1)\, \Delta_t$ matches the plane associated to $t = t_0$, it is considered that the $n_1$ succesive planes can be looped at the inlet. This works in our case as the flow, although becoming turbulent, has almost only one spatial scale associated with the hairpins. Moreover, the plane is set at the point of origin of the hairpins, a region for which the creation of secondary scales should be rather limited. The periodicity of the inlet condition built is now investigated. The error between two successive planes $n_1$ and $n$ is for which the three components of the velocity field are given is considered as follows:

$$\epsilon_1(n) = \sqrt{\sum_{j=1}^{n_y} \sum_{k=1}^{n_z} \sum_{i=1}^{3} \left(u_i^n(217, j, k) - u_i^1(217, j, k)\right)^2} \tag{2.10}$$

Let the first plane chosen (corresponding to the timestep $20550$) be refered as $1$. Figure 2.4 shows the evolution of the error $\epsilon$ against the successive time-steps. It can be seen that the best match is for $n = 406$. The error against the plane $n = 406$ is also plotted to show that the error compared to this plane has exactly the same shape for the timesteps further than the error compared to the plane $1$ at the beginning. It can also be seen that there is a slight difference between the planes $1$ and $406$, and it may lead to a slight jump in th divergence of the flow, as it has been pointed out during tests, but not enough to alter the shedding of hairpins or to see any perturbation convected in the flow. The averaged flow for $x = 12$ to $x = 20$ for the

[1] the velocity will never reach 1 exactly as the boundary layer profile converges asymptotically to 1 without ever reaching it. Some tries have been made using a connection to $U_1 = 1$ above a certain value of $y$, but this leads to a discontinuity in the velocity gradient, proven to generate a vortex sheet without physical meaning

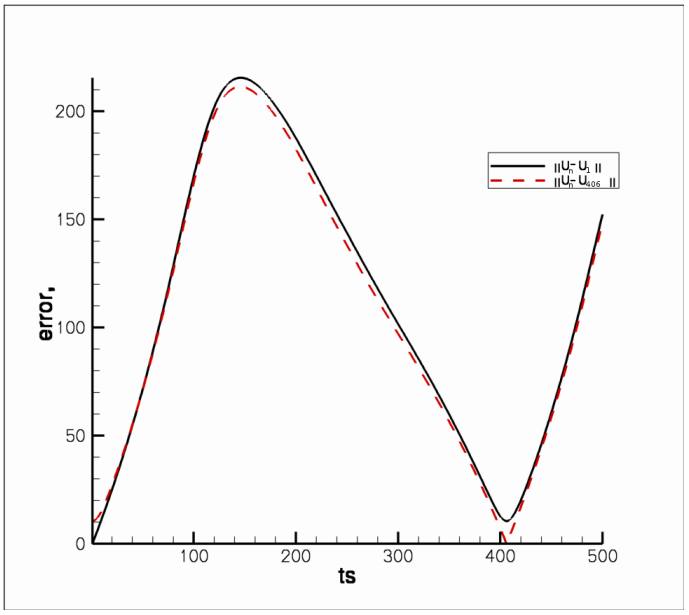


Figure 2.4: Evolution of the error between successive timesteps of the recycled inlet condition

case 1 and from $x = 0$ to $x = 8$ for the case 8 will be compared in the chapter 4. This inlet condition thus provides a clean formation and shedding of hairpins while more than doubling the speed of the simulation, which allowed much more tests on plasma actuators.

## 2.4 Evaluation of the Drag and Lift coefficients

The aerodynamical force $\mathbf{F}_A$ applied by the flow on the body arises from the constraint vector $\mathbf{T}$ distribution along the body surface $S_H$:

$$\mathbf{F}_A = \int_{S_H} \mathbf{T} dS \tag{2.11}$$

where the constraint vector is defined using the pressure field, the constraint tensor $\underline{\underline{\tau}}$ and $\mathbf{n}$ which is the surfacic unit normal vector oriented towards the fluid:

$$\mathbf{T} = \underline{\underline{\tau}}.\mathbf{n} \tag{2.12}$$

where

$$\tau_{ij} = -p\delta_{ij} + d_{ij} = -p\delta_{ij} + 2\mu\left(e_{ij} - \frac{1}{3}\Delta\delta_{ij}\right) = -p\delta_{ij} + 2\mu\left(\frac{\partial u_i}{\partial x_j} + \frac{\partial u_j}{\partial x_i}\right) \tag{2.13}$$

Then, the lift and drag coefficients $C_L$ and $C_D$ are deduced, knowing that the force exerted by the flow on the hemisphere is $-\mathbf{F}_A$:

$$C_D = \frac{4}{\rho U_\infty^2 \pi R^2} \mathbf{F}_A.\mathbf{e}_X \tag{2.14}$$

$$C_L = \frac{4}{\rho U_\infty^2 \pi R^2} \mathbf{F}_A.\mathbf{e}_Y \tag{2.15}$$

with $\mathbf{e}_X$ and $\mathbf{e}_Y$ being the unit vectors along the two directions $x$ and $y$.
Given the use of Immersed Boundary Method to define the obstacle, there is no real mesh of its surface. It is thus impossible to evaluate the surfacic integration of this vector on the hemisphere. Point values using the same kind of techniques than for the Mirror-Flow approach may be evaluated, but the surface would then have to be retriangulated to obtain the integral. A more suited approach is thus used.

The idea here is to evaluate the drag using a volumic integration of the Navier Stokes equations on a control volume $V$ including the obstacle, with boundaries matching with the cartesian grid. In order to do so, it is chosen to be the smallest box including the hemisphere and coinciding with the grid, as shown in figure 2.5. The control volume $V$ is closed by a surface $S$ which is delimited into 7 separate surfaces as

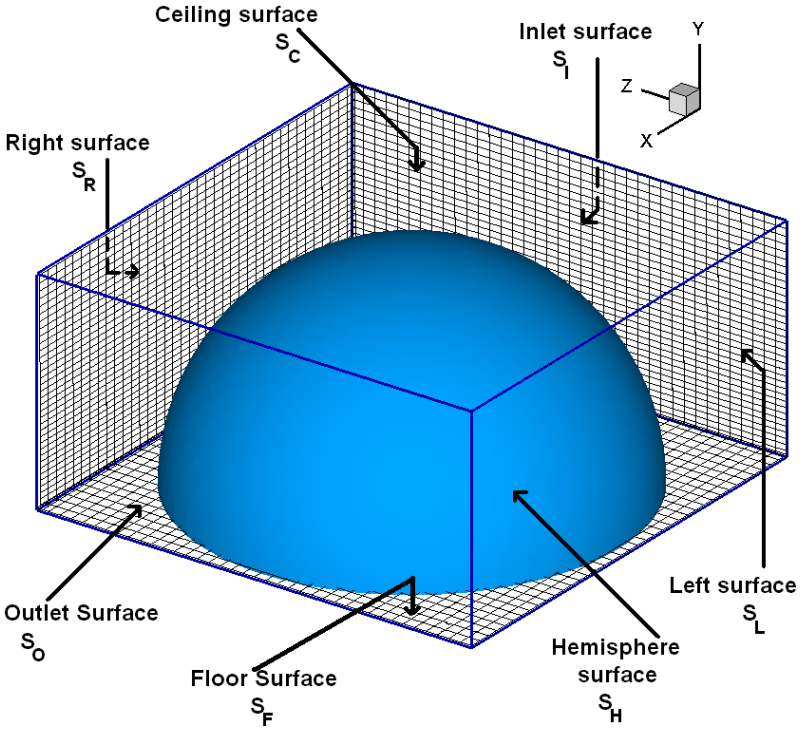


Figure 2.5: box used for the volumic integration of the Navier Stokes equations in order to obtain drag and lift coefficients

shown in figure 2.5

$$S = S_I + S_O + S_C + S_F + S_L + S_R + S_H \tag{2.16}$$

The Newton's theorem is now applied under its global form in equation 2.17 on the control volume. For the surfacic integrations below, the unit vectors on each surface are oriented towards the outside

$$\frac{D}{Dt}\int_V \rho \mathbf{u} dV = \frac{\partial}{\partial t}\int_V \rho \mathbf{u} dV + \underbrace{\int_V \rho \mathbf{u} \nabla \mathbf{u} dV}_{\mathbf{A}} = \int_S \mathbf{T} dS \tag{2.17}$$

Using the transport theorem, the term $\mathbf{A}$ can be transformed into a surfacic integration term:

$$\mathbf{A} = \int_S \rho \mathbf{u} \left(\mathbf{u}.\mathbf{n}\right) dS \tag{2.18}$$

Thus, the equation 2.17 becomes:

$$\int_V \frac{\partial \rho \mathbf{u}}{\partial t} dV + \underbrace{\int_S \rho \mathbf{u} \left(\mathbf{u}.\mathbf{n}\right) dS}_{\mathbf{B}} = \underbrace{\int_S \mathbf{T} dS}_{\mathbf{C}} \tag{2.19}$$

There is only one volumic term, and all the rest of the equations consists of surfacic terms. The contributions of the two terms $\mathbf{B}$ and $\mathbf{C}$ are now evaluated along the two principal axes, and the surfacic contributions are decomposed into 7 the partitions of $S$ given in equation 2.16:

$$\mathbf{B}.\mathbf{e}_X = -\int_{S_I} u_1^2 dS + \int_{S_O} u_1^2 dS - \underbrace{\int_{S_F} u_1 u_2 dS}_{=0} + \int_{S_C} u_1 u_2 dS$$

$$- \int_{S_R} u_1 u_3 dS + \int_{S_L} u_1 u_3 dS - \underbrace{\int_{S_H} \rho u_1 \left(\mathbf{u}.\mathbf{n}\right) dS}_{=0} \tag{2.20}$$

$$\begin{aligned}
\mathbf{B}.\mathbf{e}_Y &= - \int_{S_I} u_1 u_2 dS + \int_{S_O} u_1 u_2 dS - \underbrace{\int_{S_F} u_2^2 dS}_{=0} + \int_{S_C} u_2^2 dS \\
&\quad - \int_{S_R} u_2 u_3 dS + \int_{S_L} u_2 u_3 dS - \underbrace{\int_{S_H} \rho u_2 \left(\mathbf{u}.\mathbf{n}\right) dS}_{=0}
\end{aligned} \tag{2.21}$$

$$\begin{aligned}
\mathbf{C}.\mathbf{e}_X &= -F_D + \int_{S_I} \left( p - 2\mu \frac{\partial u_1}{\partial x} \right) dS - \int_{S_O} \left( p - 2\mu \frac{\partial u_1}{\partial x} \right) dS - \int_{S_F} \mu \frac{\partial u_1}{\partial y} dS \\
&\quad + \int_{S_C} \mu \left[ \frac{\partial u_1}{\partial y} + \frac{\partial u_2}{\partial x} \right] dS - \int_{S_R} \mu \left[ \frac{\partial u_1}{\partial z} + \frac{\partial u_3}{\partial x} \right] dS + \int_{S_L} \mu \left[ \frac{\partial u_1}{\partial z} + \frac{\partial u_3}{\partial x} \right] dS
\end{aligned} \tag{2.22}$$

$$\begin{aligned}
\mathbf{C}.\mathbf{e}_Y &= -F_L - \int_{S_I} \mu \left[ \frac{\partial u_1}{\partial y} + \frac{\partial u_2}{\partial x} \right] dS + \int_{S_O} \mu \left[ \frac{\partial u_1}{\partial y} + \frac{\partial u_2}{\partial x} \right] dS - \int_{S_F} \left( -p + 2\mu \frac{\partial u_2}{\partial y} \right) dS \\
&\quad + \int_{S_C} \left( -p + \mu \frac{\partial u_2}{\partial y} \right) dS - \int_{S_R} \mu \left[ \frac{\partial u_2}{\partial z} + \frac{\partial u_3}{\partial y} \right] dS + \int_{S_L} \mu \left[ \frac{\partial u_2}{\partial z} + \frac{\partial u_3}{\partial y} \right] dS
\end{aligned} \tag{2.23}$$

There is a minus sign in front of $F_D$ and $F_L$ in the equations 2.22 and 2.23 as the unit normal vectors $\mathbf{n}$ are oriented here towards the hemisphere. Then, replacing the relations obtained in equations 2.20, 2.21, 2.22 and 2.23 into the equation 2.19:

$$\begin{aligned}
F_D &= - \int_V \frac{\partial}{\partial t} \left( \rho u_1 \right) dV + \int_{S_I} u_1^2 dS - \int_{S_O} u_1^2 dS - \int_{S_C} u_1 u_2 dS + \int_{S_R} u_1 u_3 dS \\
&\quad - \int_{S_L} u_1 u_3 dS + \int_{S_I} \left( -p + 2\mu \frac{\partial u_1}{\partial x} \right) dS - \int_{S_O} \left( -p + 2\mu \frac{\partial u_1}{\partial x} \right) dS + \int_{S_F} \mu \frac{\partial u_1}{\partial y} dS \\
&\quad - \int_{S_C} \mu \left[ \frac{\partial u_1}{\partial y} + \frac{\partial u_2}{\partial x} \right] dS + \int_{S_R} \mu \left[ \frac{\partial u_1}{\partial z} + \frac{\partial u_3}{\partial x} \right] dS - \int_{S_L} \mu \left[ \frac{\partial u_1}{\partial z} + \frac{\partial u_3}{\partial x} \right] dS
\end{aligned} \tag{2.24}$$

$$\begin{aligned}
F_L &= - \int_V \frac{\partial}{\partial t} \left( \rho u_2 \right) dV + \int_{S_I} u_1 u_2 dS - \int_{S_O} u_1 u_2 dS - \int_{S_C} u_2^2 dS + \int_{S_R} u_2 u_3 dS \\
&\quad - \int_{S_L} u_2 u_3 dS + \int_{S_I} \mu \left[ \frac{\partial u_1}{\partial y} + \frac{\partial u_2}{\partial x} \right] dS - \int_{S_O} \mu \left[ \frac{\partial u_1}{\partial y} + \frac{\partial u_2}{\partial x} \right] dS + \int_{S_F} \left( -p + 2\mu \frac{\partial u_2}{\partial y} \right) dS \\
&\quad - \int_{S_C} \left( -p + \mu \frac{\partial u_2}{\partial y} \right) dS + \int_{S_R} \mu \left[ \frac{\partial u_2}{\partial z} + \frac{\partial u_3}{\partial y} \right] dS - \int_{S_L} \mu \left[ \frac{\partial u_2}{\partial z} + \frac{\partial u_3}{\partial y} \right] dS
\end{aligned} \tag{2.25}$$

For each of the surfacic integrals in equations 2.25 and 2.24, in order to avoid overlaps of the nodes contributions, the integration is done surfacic cell by surfacic cell. Given a rectangular cell with four nodes (1 to 4) and two lengths a and b over its two directions (all the cells are rectangular as the mesh is cartesian), and using bilinear interpolation along the element:

$$\int_{cell} f dS = \frac{f_1 + f_2 + f_3 + f_4}{4} ab \tag{2.26}$$

The only remaining term to evaluate the lift and the drag is thus the contribution of the eulerian acceleration terms

### Evaluation of the contribution of the eulerian acceleration terms

As for the surfacic integration, the evaluation is done element by element. It is only problematic when the considered cell is partially cut by the virtual boundary of the obstacle.
When the cells are far enough to be completely in the flow zone, the contribution of the element is easily evaluated: considering an 8 nodes parallelepiped cell with lengths a, b and c along the three directions, and

using bilinear interpolation inside the element, we get:

$$\int_V f dV = \frac{abc}{8} \sum_{i=1}^{8} f_i$$

But it is far more complicated when the surface intersects the element. The first step of the method is thus to distinguish these two families of elements. For that, the radius for each node of the considered element is compared to the radius of the sphere.

- If all the nodes are outside, it is considered that the element is completely outside the obstacle (it may not be true on top of the sphere, for instance, if the mesh is too coarse, but the meshes involved here are considered refined enough to neglect that kind of cases)
- If at least 7 nodes are in the obstacle, the contribution of the element is neglected.
- Between 1 and 6 nodes, the cell is considered as partially immerged, and its volume is approximated as described below

When a cell is partially immerged, the procedure to evaluate its contribution is the following

1. Find all the edges that are cut by the surface by comparing the sign of $r - R$ ($r$ the local radius and $R$ the radius of the hemisphere) at their two extremities.
   (a) if the edge is cut, the length between the extern extremity and the hemisphere over this edge is evaluated as the length associated to the edge
   (b) otherwise, the associated length is set to the length of the edge
2. For the 4 edges on the same direction, the max and min are evaluated
3. The volume of the element is equal to

   $$\frac{1}{8} \times (max_x + min_x) \times (max_y + min_y) \times (max_z + min_z)$$

   This expression is more or less accurate considering the way the cell is cut and is far from being optimal, but is simple and accurate enough considering that the acceleration will tend to zero at the boundary, and that most of the cells of the domain are either completely immerged or not.
4. Once the volume evaluated, it is multiplied by the sum of all the accelerations at the nodes of the element that are outside the hemisphere and divided by 8, the usual number of nodes on an element.

This loop is done over all the cells inside the domain.

## 2.5 Evaluation of the unsteady Lagrangian acceleration

In order to study locally the zones of dissipation and production associated to the flow, using Newton's theorem defined in equation 2.17, the Lagrangian accelaration has to be evaluated. As far as the Eulerian part is concerned, as simple first-order finite difference approximation is performed, using the velocity fields at the beginning of the time step and the velocity computed after the three sub-steps performed:

$$\frac{\partial \mathbf{U}}{\partial t} \approx \frac{\mathbf{U_{i+1}} - \mathbf{U_i}}{\Delta t}$$

It is not consistent with the finite-difference schemes used for spatial derivation, which are sixth-order, but increasing the order would lead to the storage of the complete velocity field for the several previous time-steps, and the first order is a way to get a good approximation while maintaining low storage. Moreover, the convective part of the acceleration should dominate in our case. The convective term is evaluated at each sub-step, and the latest approximation is used to obtain the remaining part of the acceleration field.
The pressure gradients also have to be exported as the ratio of this terms by the acceleration field is a pertinent indicator of the local nature of the flow (its dissipation rate, for instance).

## 2.6 Statistics

### 2.6.1 Mean and RMS quantity evaluations

The mean quantities for every variable will be refered using capital letters. For each simulation performed, the mean velocities $U_i$ and Lagrangian accelerations $A_i$ are evaluated, as well as the components of the Reynolds tensor $\overline{u_i u_j}$. Using these components, two other physical quantities relative to turbulence are evaluated: the turbulent kinetic energy (TKE) $k$ and the turbulent production $P_k$:

$$k = \frac{1}{2}\left(\overline{u_1^2} + \overline{u_2^2} + \overline{u_3^2}\right) \tag{2.27}$$

$$P_k = -\overline{u_1 u2}\frac{\partial u_1}{\partial y} \tag{2.28}$$

For the simulation $20 \times 10 \times 5$, the first and second order moments are also evaluated for the pressure gradient. The table 2.6.1 provides for each simulations where statistics has been performed the starting time-step for time averaging, the averaging time, and the values evaluated. The time step for all the simulations is set to $\Delta_t = 1 \times 10^{-2}$ The usual averaging time is $4000\Delta_t = 40$, which has been tested to be enough to

| | Case name | $U_i$ | $\overline{u_i u_j}$ | $A_i$ | $P_i$ | $\overline{p_i p_j}$ | Probes | Probe time(ts) | Averaging start(ts) | Averaging time(ts) |
|---|---|---|---|---|---|---|---|---|---|---|
| 1 | $20 \times 10 \times 5$ | × | × | × | × | × | × | 10000 | 16550 | 4000 |
| 2 | $20 \times 10 \times 10$ | × | × | × | | | × | 12000 | 18550 | 4000 |
| 3 | $30 \times 10 \times 5$ | × | × | × | | | | | 8000 | 4000 |
| 4 | $20 \times 10 \times 5 - H = 1.5$ | × | × | × | × | × | × | 8000 | 4000 | 6000 |
| 5 | $20 \times 10 \times 5 - H = 1$ | | | | | | | | | |
| 6 | $20 \times 10 \times 5 - 750$ | | | | | | | | | |
| 7 | $20 \times 10 \times 5 - 500$ | | | | | | | | | |
| 8 | Inlet-validation | × | × | × | | | | | 4000 | 4000 |
| 9 | 2D-actuator | × | × | | | | | | 4000 | 4000 |
| 10 | Blasius forcing | × | × | | | | | | 4000 | 4000 |
| 11 | 3D-actuator | × | × | × | | | | | 6000 | 4000 |
| 12 | Hairpin forcing | × | × | × | | | | | 6000 | 4000 |

Table 2.2: Table of the statistics performed and their associated parameters

get convergence of the first and second order moments. The two first cases have been run for much longer than the others as they will be the cases on which most of the dynamical studies will be performed.

### 2.6.2 Boundary layer related statistics

In order to characterize the transition of the boundary-layer from laminar to turbulent, some other quantities are evaluated: the displacement and momentum thickness as well as their ratio:

$$\delta = \int_0^\infty \left(1 - \frac{U_1}{U_\infty}\right) dy \tag{2.29}$$

$$\theta = \int_0^\infty \frac{U_1}{U_\infty}\left(1 - \frac{U_1}{U_\infty}\right) dy \tag{2.30}$$

$$\tag{2.31}$$

The ratio $\delta/\theta$ is an indicator of the nature of the boundary-layer. A value around $2.4$ is typical of a laminar boundary layer while a value of $1.5$ indicates a turbulent boundary-layer. It also has to be pointed out that this ratio will diverge in case of a separation or reattachement line.

### 2.6.3 Export of probes

An routine has been added to the code in order to be able to export unsteady values at different locations of the flow. So, at every time-step, the three components of the velocity, acceleration and pressure gradients are exported in $444$ locations of the flow[2]. The figure 2.6 gives two views in both iso-X and iso-Z planes of the position of all the probes as well as the mean $U_1$-velocity in the corresponding slice plans ($X = 7$, middle of the sphere, and $Z = 0$, symmetry plane). This probes will also be used to study the dynamics of the flow and evaluate, for instance, the Strouhal number associated to the hairpin shedding using autocorrelations, as well as the convection speed of the hairpins using spatial intercorrelation. The recirculation zone is strongly

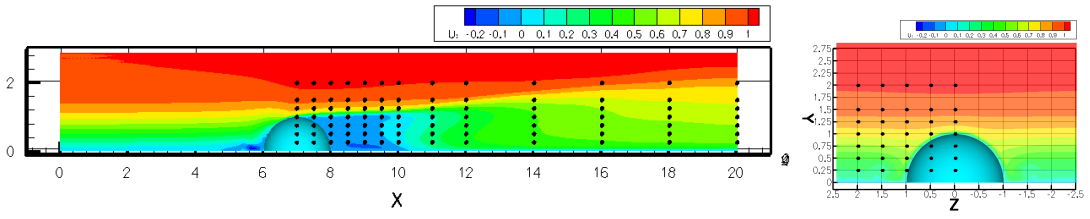


(a) (b)

Figure 2.6: Views of the position of all the probes as well as the mean U-velocity in the corresponding slice plans in both iso-X (a) ($X = 7$) and iso-Z planes (b) ($Z = 0$)

discretized as it should be the most perturbated zone of the flow. Then lines of probes are defined along the three directions. It is thus possible to follow the path of the hairpins and to realise spatial correlations. As the hairpins are supposed to move upwards when being convected, probes are set at a maximum height of $2$. Only half of the domain is covered along the cross-stream direction (z), given the strong symmetry of the flow. A validation of this symmetry has been performed by taking the difference between left and right sides of the median plane for a given time-step, leading to a zero close to machine accuracy.

[2] in order to avoid slowing down the code, the export to files is only made every $100$ timesteps

# Chapter 3

# Flow around hemispheres

## 3.1 Generation of hairpin vortices

According to [1], the hairpin are generated by the accumulation of vortex sheet lines in front and on the sides of the hemisphere. The figure 3.1.(a) is a sketch extracted from their articles illustrating the formation process, while the figure 3.1.(b) shows an unsteady visualisation of the standing vortex and a shed hairpin, using isosurfaces of the $Q$ criterion.

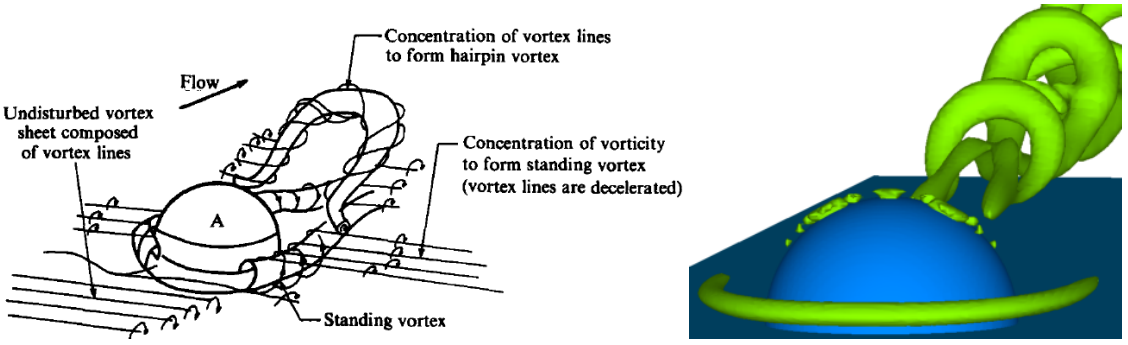


(a) (b)

Figure 3.1: (a): Formation of hairpin vortices and standing vortices due to the concentration of vortex lines, extracted from [1]. (b):visualisation of the unsteady $Q = 1.5$ criterion isosurface for $Re_\tau = 1000$ and $H = 2$

The representation 3.1.(a) has been obtained by analyzing the hydrogen bubble injection visualisations and is in good agreement with the unsteady visualisation provided in figure 3.1.b. According to [1], the accumulation of vortex lines leads to the creation of hairpin vortices as well as a standing vortex which surrounds the hemisphere. One may also wonder what may be the role played by the pressure and vorticity fields, especially in the wake in this shedding. And apart from the fact that the so-called standing vortex is always present around the hemisphere, one may wonder if this structure is fluctuating in time, and thus playing a role in the shedding mechanism.

#### Shedding frequency evolution with $Re$

[1] have studied the evolution of the shedding frequency with the Reynolds number, using several incoming speeds, three different sphere radius, and three different downstream localisations (it modifies the height ratio $H$) in order to cover a broad set of Reynolds number ($30 \leq Re \leq 3400$). Below the value of 120, the flow is steady, and the shedding becomes unstable over 3400. The evolution of the shedding frequency with the Reynolds number may come with some regime changes. It has not been clearly documented for

the hemisphere on a flate plate, but the transition from steady to unsteady flow has been described on the sphere by [19]. The figure 3.2 shows three successive isosurfaces of streamwise vorticity for Reynolds numbers below and above the transition number, an equivalent study for the hemisphere will be tried to locate the more accurately possible the transition of the flow. Below the transition, the sphere generates two

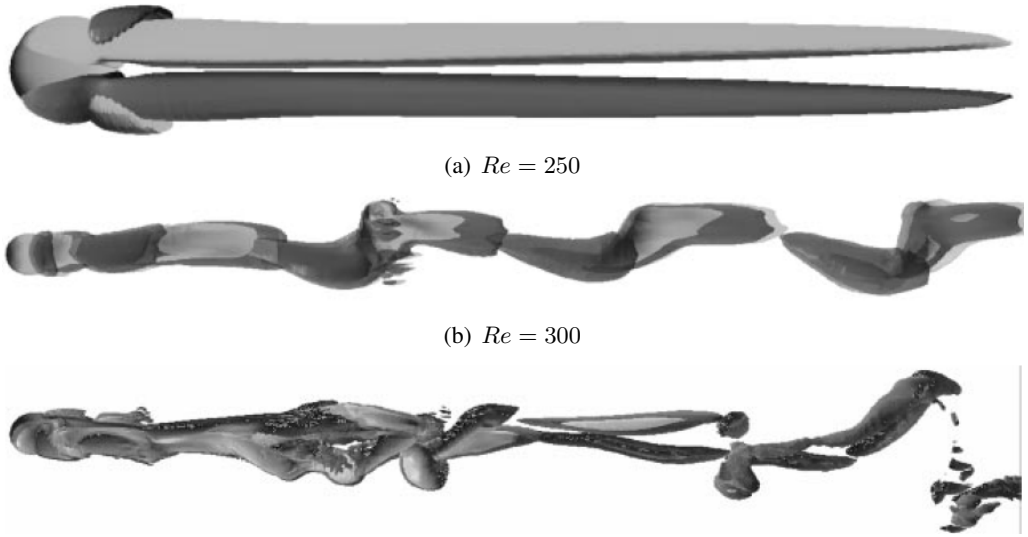

(a) $Re = 250$

(b) $Re = 300$

(c) $Re = 500$

Figure 3.2: Evolution of the streamwise vorticity isosurfaces characterizing the shedding regimes around the transition from steady to unsteady, extracted from [19]

kinds of steady streamwise vortices, and above, the hairpin shedding process starts. Given the presence of a stabilizing standing vortex around the hemisphere, this transition may occur later, as it will be shown in the next sections.
[1] found that the hairpin shedding starts around $Re = 120$ and becomes unstable for $Re = 3400$. As Direct Numerical Simulations are performed, reaching $Re_\tau = 1000$ is sufficient. [9], for instance, do not go further than $Re_\infty = 750$ with $H = 1.2$, leading to a Reynolds number $Re_\tau = 725$.

The Strouhal number associated to this shedding process has been systematically measured for all the configurations and the results can be seen on figure 3.3.(a)-(b), as well as a similar evolution obtained numericaly by [9] for $Re_\infty \in [400, 700]$ ($Re_\tau \in [387, 677]$ with $H = 1.2$). Even though [1] is rather qualitative, the insights given on the shedding/generation process offer a lot of data that will be used to validate our flow before trying any control process. Figure 3.3.(c) is more accurate for the domain concerned, but in the study performed here, the height ratios are usually higher than 1.2 leading to too many secondary structures generated by the hairpins at higher Reynolds number.

### 3.1.1 Link between successive hairpins

The relation between consecutive hairpins is now investigated. The figure 3.4.a shows a scheme of the interaction between these consecutive hairpins and the way they coalesce by [1], while the figure 3.4.b shows an unsteady visualisation of this same relation between two successive hairpins extracted from [9] The head shapes implies that it contains both streamwise and transverse vorticity, while the leg is more dominated by streamwise vorticity. The figure 3.4 shows that the legs of the older loops are caught in the deforming layers of the previous ones. But as the shedding frequency varies with $Re$, it may be possible to get regime with a stronger separation of consecutive vortices and prevent them from coalescing. The fact that the legs get away from the symmetry plane in the end seems to be caused by the down-flow generated by the head of the following hairpin.

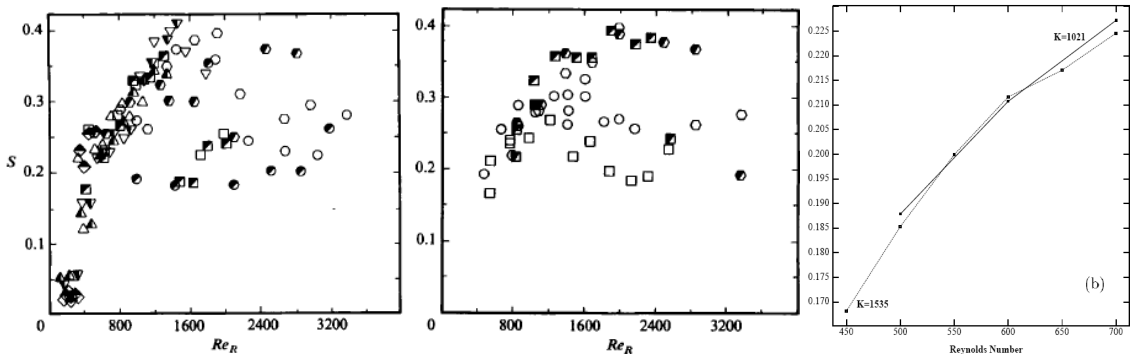


(a) (b) (c)

Figure 3.3: Evolution of the shedding Strouhal Number S with $Re$ and $H$, extracted from [1] (a and b, for several different height ratios $H$), and from [9]($H = 1.2$).

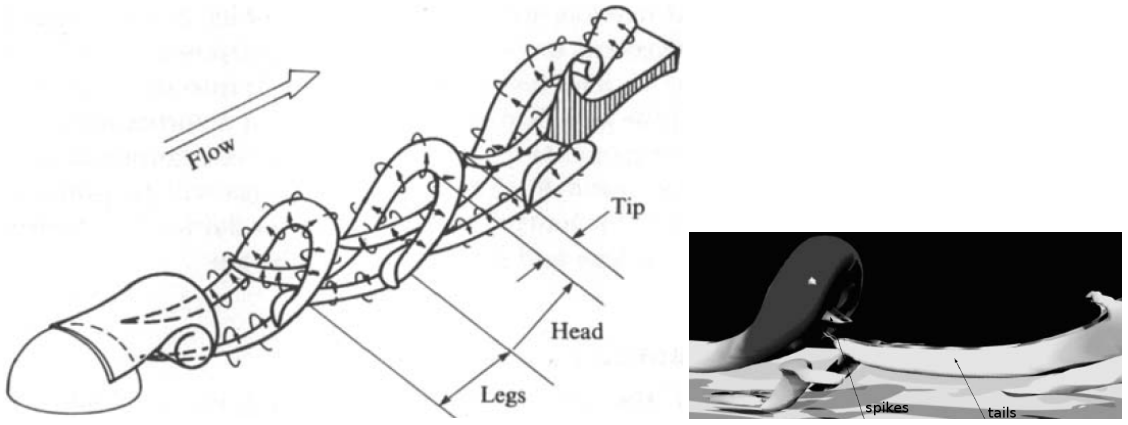


(a) (b)

Figure 3.4: Scheme (a, from [1]) and unsteady visualisation (b, from [9], with $Re = 670$, and $\lambda_2 = -1$) of the relation between consecutive hairpins

The visualisation in fig. 3.4.b shows that the leg of the hairpin seems to be disconnected from the part included in the following hairpin, called here the spikes. According to the scheme in fig. 3.4.a, these "spikes" are connected to the legs, but [9] quote that they appear simultaneously without link, and are thus separated structures, but one may wonder if it is not just a treshold problem in the definition of the isosurface leading to this separation, as the separation zone is where the effect of the next hairpin tail is maximal. This question will be investigated in the next section. Moreover, a "vortex bridge" can be seen on the right-side of the picture, showing a reconnection between the two legs of the hairpin. This structure is said to have a very short life length and to be a common form of vortex reconnection in viscous flows according to [9]. It will however not be noticed in our simulations, and thus might only occur at lower height ratios than those investigated in the present study.

The relation between consecutive vortices as well as their evolution with the Reynolds number will be briefly investigated in the next sections of this study.

# Chapter 4

# Results

The mesh resolution has been defined in the last chapter. The length of the domain along the $y$ direction is fixed to $L_y = 10$ and will not be modified. As this is the direction where the mesh is coarsened, it is the most cost effective way to lower the blockage ratio. The variables left are the width $L_z$, which will characterise the effect of the blockage ratio on the flow, the length $L_x$ to determine the effect of the outlet condition on the flow, the Reynolds number $Re_\tau$ and the aspect ratio $H$. The idea of this parametric study is to evaluate the effect of this different parameters on the physics of the flow.

The blockage ratio as well as the length of the domain may have an effect in the way the boundary-layer recovers from this shedding and on the way the transition to a turbulent boundary layer may occur. The perturbation of an initially laminar boundary layer results, for given Reynolds numbers and heigth ratio, in the creation of a kind of structures that is present on fully turbulent boundary layers, and it may be interesting to see if this add is enough to generate a transition towards a turbulent boundary layer, and to what extent the different parameters chosen have an effect on this supposed transition.

As far as the shedding process is concerned, [9] and [1] have already exhibited the modification of the Strouhal number with the Reynolds number, and changing the heigth ratio or the blockage ratio, generating higher velocities around the hemisphere, should also imply Strouhal modification. The way the shedding process is modified is also to be investigated. Does a change in the blockage ratio lead to less periodical shedding, and lower first peak autocorrelation values? [1] have also pointed out the progressive apparition of secondary structures when increasing the Reynolds number, and finding out if a similar effect occur when the heigth ratio is modified may also be of interest.

And in order to test the plasma actuators, the nature of the flow and its variations with the parameters above must be investigated in order to define a proper benchmark case.

## 4.1 Effect of the blockage ratio

In this section, the $20 \times 10 \times 5$ and $20 \times 10 \times 10$ simulation results are compared (1 and 2, or high and low blockage respectively). The blockage ratios for these two domains as well as previous experiments and simulations are summed up in table 4.1

### 4.1.1 Comparaison of snapshots

This first subsection is highly qualitative. Figure 4.1 shows for the two cases the isosurfaces of the $Q$ criterion for a treshold value of $1.5$ representing the hairpins. This two snapshots are not time-correlated[1], and the only information that can be gathered from this configuration concerns the shape of the hairpins.

[1] it will be seen further that the two cases have not the same Strouhal number, leading to a loss of correlation

| Associated article | Radius | Domain size (cartesian) | Domain size (cylindrical) | Blockage |
|---|---|---|---|---|
| Experiments | | | | |
| [1] | $\leq$ 18mm | $2.5 \times 0.85 \times 0.25$m | | $\leq 0.24\%$ |
| Simulations | | | | |
| [19] | 1 | | $18 \times 9$ | $1.\%$ |
| [9] (coarse) | 1 | $38.4 \times 12.8 \times 6.5$ | | $1.9\%$ |
| [9] (fine) | 1 | $40 \times 16.8 \times 8$ | | $1.15\%$ |
| Actual simulation (1) | 1 | $20 \times 10 \times 5$ | | $3.14\%$ |
| Actual simulation (2) | 1 | $20 \times 10 \times 10$ | | $1.57\%$ |

Table 4.1: Blockage ratio for several experiments and simulations around a sphere or an hemisphere

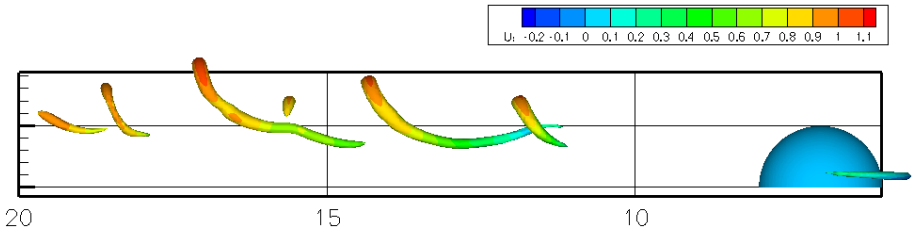


(a) 20x10x5 lateral

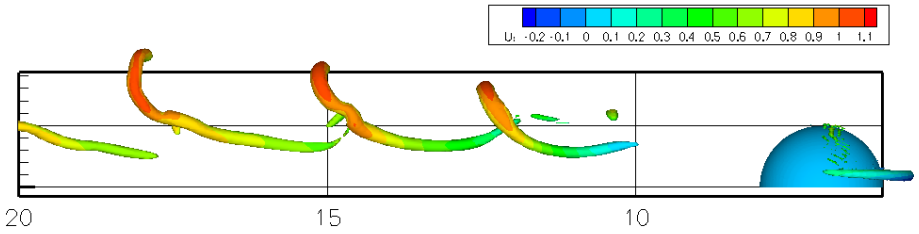


(b) 20x10x10 lateral

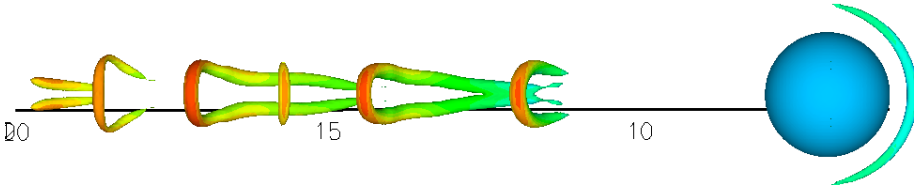


(c) 20x10x5 top

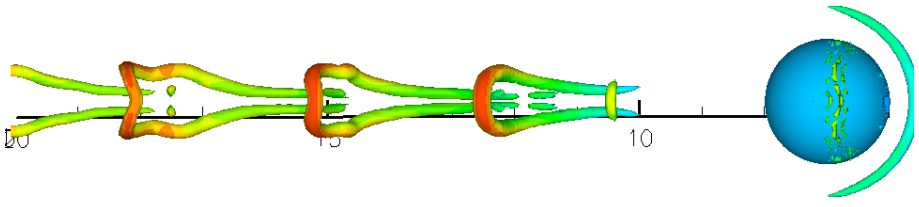


(d) 20x10x10 top

Figure 4.1: Lateral and top screenshots of the hairpins using ($Q = 1.5$) for both cases along the cross-flow direction. The isosurfaces are colored using the x-velocity

It appears that the hairpins are more similar to one another in the low-blockage case street. Each hairpin seems to the growth of the previous one, unlike the high-blockage case where some hairpins have no leg for

this level of $Q$. Moreover, some secondary structures appear on figure 4.1.(a) and (c) (for instance, a cross stream structure above the legs of the second hairpin). The distance between two successive hairpin heads also seems to be more constant for the case 2. Finally, the shedding frequency appears to be a little lower for the low-blockage case.
One can also point out the presence of secondary structures refered as "'spikes"' by [9], which are in the continuity of the legs and appear under the head of the following hairpin. They do not seem yet to be in the same plane as the end of the legs, and thus seem to be separated as supposed by [9].
Finally, the progression of the hairpin upwards is almost linear along the streamwise direction for the low-blockage case, while the high-blockage does only get a linear progression for the first three hairpins. One may though wonder if it is not a consequence of the outlet boundary condition. The informations gathered here are highly dependant on the snapshot chosen, and thus, the statistics of the flow will now be compared.

### 4.1.2 Comparaison of the two simulations statistics

#### Comparaison of the mean velocities

In order to characterize the hairpins street as well as, for instance, the size of the recirculation bubble, most of the comparaisons will be performed on the median plane. Figure 4.2 gives successive $U_1$ profiles for different $x$ positions in the median wake of the hemisphere.

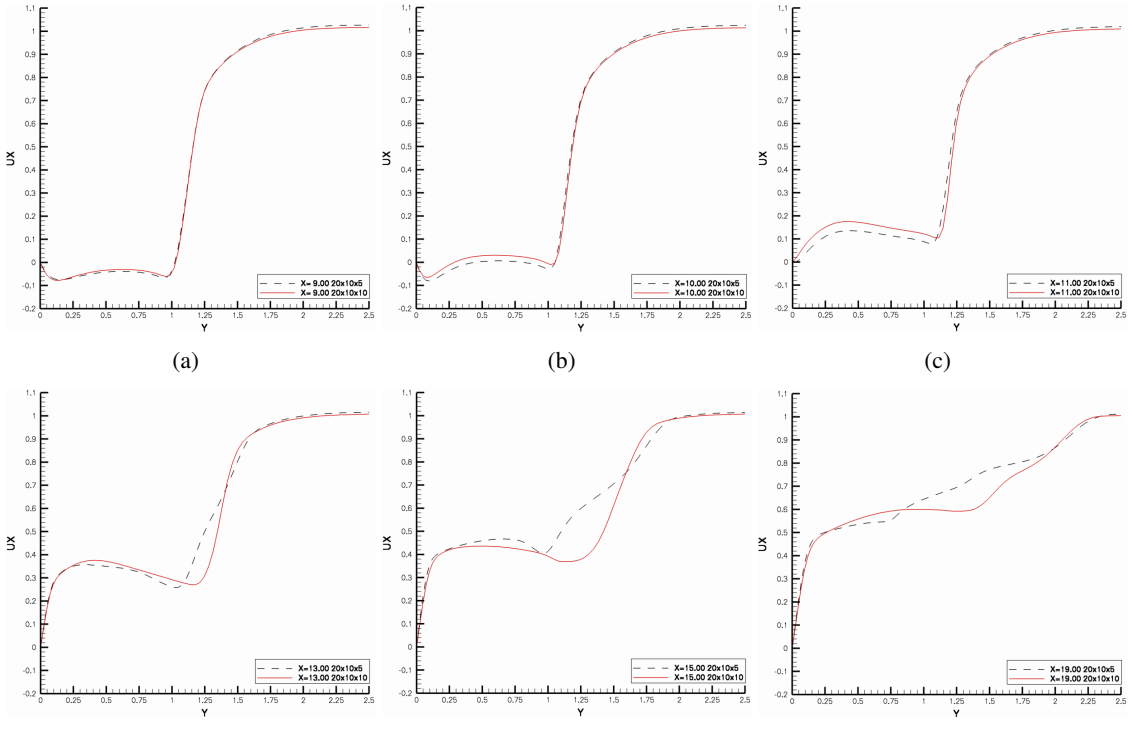


(a) (b) (c)

(d) (e) (f)

Figure 4.2: $U_1$ profiles for $x = \{9, 10, 11, 13, 15, 19\}$ in the median wake of the hemisphere

- Figures 4.2.(a)-(f) show that the $20 \times 10 \times 5$ velocities are always higher when getting out of the boundary-layer, around $y = 2$.
- Figure 4.2.(a) shows that both results appear highly identical in the near wake, with the presence of a recirculation zone for $y < 1.1$. This recirculation height is the same in figure 4.2.(b), although the $20 \times 10 \times 10$ profile starts to exhibit positive values in the wake. As both profiles are strictly positive in figure 4.2.(c), the recirculation length seems to be a little shorter in the $20 \times 10 \times 10$ case, and both of them are between $x = 10$ and $x = 11$

- Figures 4.2.(a)-(b) also show that the profiles have two minimums, one close to the wall and the other close to 1 and a maximum around $y = 0.5$ which is not the typical form for a recirculation bubble. It seems that the secondary maximum for $y = 1$ is linked to the hairpin heads: the clockwise rotation along the crosstream direction should lead to the presence of a minimum of velocity, then a maximum, which seems to be hidden by the increase of velocity due to the boundary layer. It explains why the recirculation bubble has not the typical shape that could occur, for instance, behind a step.

- Figures 4.2.(b)-(f) show that the hairpin-head associated minimum of velocity for the $20 \times 10 \times 10$ case is getting away from its $20 \times 10 \times 5$ equivalent by moving upwards faster. It can also be noticed that it spreads into a smooth minimum with $x$ while its equivalent for the high-blockage ratio remains sharper. It seems that the high-blockage case generates stronger boundary-layer associated $U_1$ velocities that tend to hide this minimum which is almost invisible in figure 4.2.(f). It also explains why in figure 4.1.(a), the hairpins are less visible close to the end of the domain. It thus seems that in the high-blockage simulation, the flow goes back faster to a boundary-layer-like profile.

- Figures 4.2.(c)-(f) also exhibit for both simulations the presence of a strong linear shear for $y < 0.1$, as if a new boundary layer was created at the exit of the recirculation bubble.

The $U_1$ velocity is now plotted along the $y$ direction in the median wake of the hemisphere in figure 4.3: It can be seen on figures 4.3.(a)-(b) that the recirculation length is shorter for the $20 \times 10 \times 10$ case, while

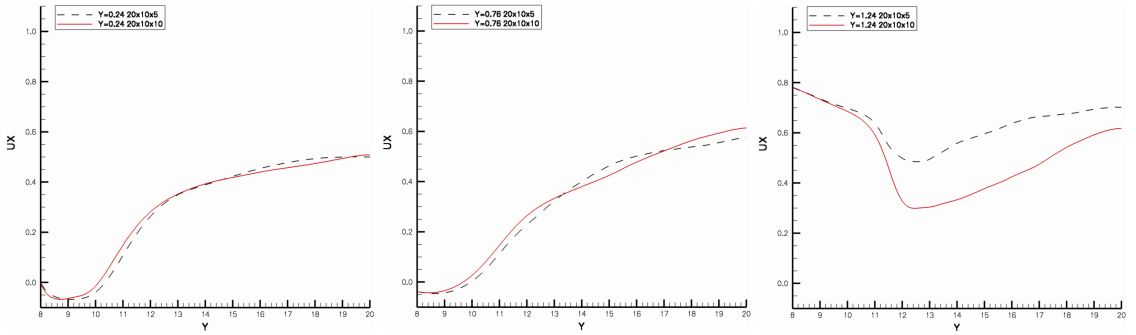


(a) (b) (c)

Figure 4.3: $U_1$ profiles for for $y = \{0.25, 0.75, 1.25\}$ in the median wake of the hemisphere

the figure 4.3.(c) shows that although the flow is similar for $x < 11$, the higher velocities generated by a more blocked boundary-layer around the hemisphere lead to a strong difference below that point, even if this error decreases with $y$ for $y > 1.5$.

### Comparaison of the second order moments

Figure 4.4 shows the contours of turbulent kinetic energy $k$ on the median plane for both simulations. The path used by the hairpin heads leads to turbulent kinetic energy as it is the region where $u_1$ and $u_2$ will get the stronger oscillations.

- The beginning of non-zero $k$ values occurs before for the $20 \times 10 \times 5$ case, around $x = 11$ while it starts at $x = 12$ for the low-blockage grid. In both case, the first non-zero value is around $y = 1.1$

- Similarly, the maximum value occurs further downstream at $x = 15.7$ for the low-blockqge mesh compared to the $x = 13.4$ when there is an high-blockage. It may be due to the fact that the growing absolute instability generated by the hemisphere is fed with more energy due to higher velocities on top of the hemisphere for the high-blockage ratio, leading to an earlier setting of the resulting hairpins.

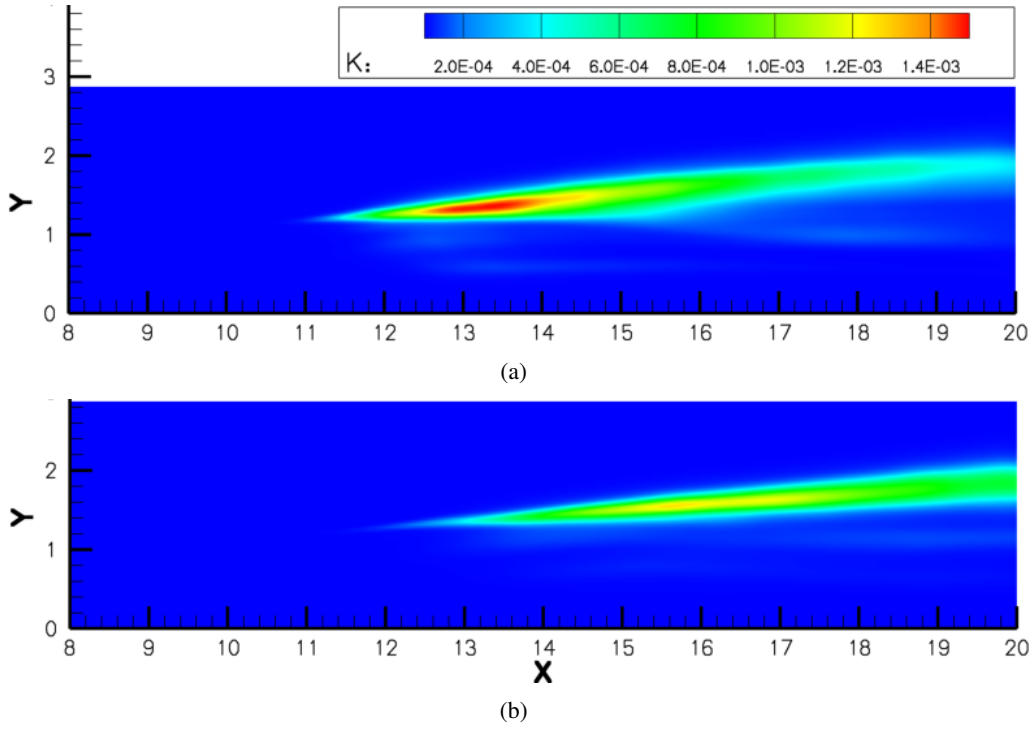


(a)

(b)

Figure 4.4: Contours of $k$ in the median plane for the $20 \times 10 \times 5$ (a) and $20 \times 10 \times 10$ (b)

- It can also be seen that the spreading of TKE starting from the hairpin heads pathline is stronger for the high-blockage case, with stronger maximum values too, while the pathline grows almost linearly and symmetrically above and below for the low-blockage mesh.
- Close to the outlet, the TKE peak has almost disappeared in figure 4.4.(a), being almost totally diffused, while the thickness of the non-zero contours keeps increasing in figure 4.4.(b)
- In both cases, the hairpin heads characterised by the maximum of $k$ follow a linear upwards line, as exhibited by [1].
- One can also point out for both cases the presence of a secondary maximum for $y \approx 1$ and $x > 17$.

In order to study more closely the evolution of the TKE peak and its spreading, figure 4.5 shows for both cases a serie of profiles of $k$ for different $x$ locations.

- Figure 4.5.(a) shows that the $k$ peak is maximal for $x = 13$ then decays while spreading in an unsymmetric way, with a slower decrease on the floor side that in the ceil side, as seen in figure 4.4.(a). Oppositely, for the low-blockage case, the maximum is to be found for the $x = 17$ profile. The peak first grows till this value, keeping the same slope, then starts spreading for the last profile $x = 19$. It thus appear that, as expected earlier, there is a spatial delay between the behaviour of the two cases with a later maximum leading to a later decrease and spreading in the low-blockage case.
- Figure 4.5.(a)-(b) also show that the maximum level of $k$ in the last profiles is twice lower for the high-blockage case. It corresponds to the supposition made earlier according to which the transition from a laminar flow with an unique scale-length associated to the hairpin shedding to a boundary-layer which is a good model for a turbulent boundary-layer is occuring further upstream for the high-blockage case, due to higher velocities around the hemisphere.

In order to study the reason why the two $k$ peaks are differents, profiles of the production term $P_k = -\overline{u_1 u_2}\frac{\partial U_1}{\partial y}$ are now exhibited in figure 4.6 Figure 4.6 shows that for every position $x$, the $20 \times 10 \times 10$ grid is associated with higher (though sharper) peaks of $P_k$, with an higher integral value over the profile. It thus shows that even though the transition towards a turbulent boundary-layer seems to appear earlier for high blockage ratios, the transition speed should be faster for the $20 \times 10 \times 10$ case.

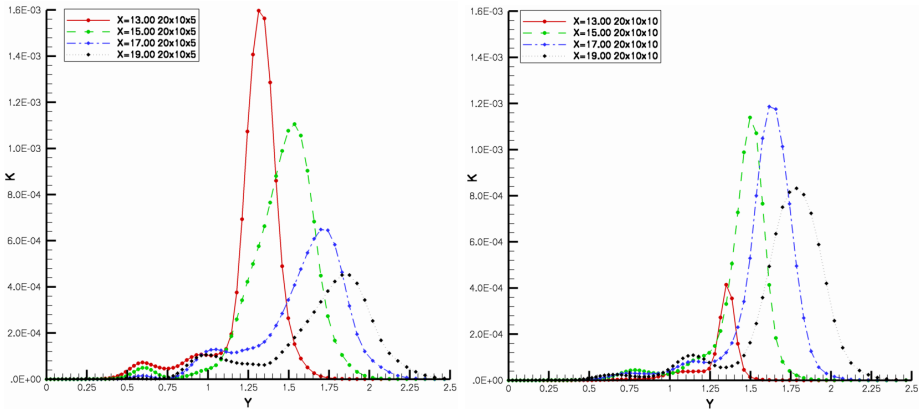


(a) (b)

Figure 4.5: $k$ profiles for $x = \{13, 15, 17, 19\}$ in the median wake of the hemisphere for the high (a) and low (b) blockage grids

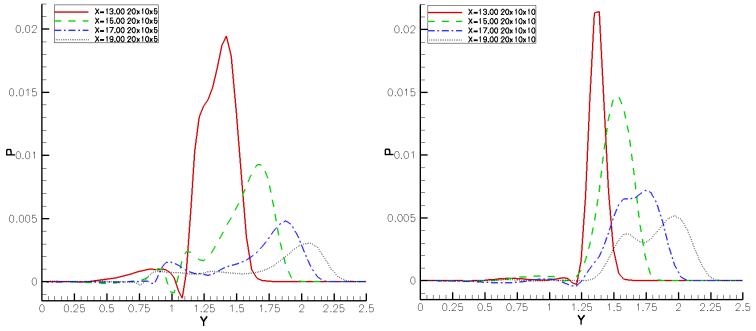


(a) (b)

Figure 4.6: $P_k = -\overline{u_1 u_2}\frac{\partial U_1}{\partial y}$ profiles for $x = \{13, 15, 17, 19\}$ in the median wake of the hemisphere for the high (a) and low (b) blockage grids

### Comparaison of boundary-layer related statistics

Figure 4.7 shows the evolution of the displacement and momentum thickness as well as their ratios on the median plane for both cases. Figure 4.7.(c) shows that the transition to turbulence is first faster for the high-blockage grid, and goes below $2.4$ faster, which indicates that the boundary layer is no longer laminar. But it then converges to a value of $1.8$, which corresponds only to a partial transition, while the progression of the ratio $\frac{\delta}{\theta}$ does not lead to convergence, and even to lower values $x > 18$ with a low-blockage gird. It thus appear that the blockage ratio makes the transformation towards a turbulent-like boundary layer start earlier, but does not lead to a complete transition while the low-blockqge has a smoother transition but ending up more advanced at the end of the domain, which is consistent with the profiles shown on figures 4.6.(a)-(b) or the median $k$ contours in figures 4.4.(a)-(b) showing that the production stops and that the production of $TKE$ slows down approaching the outlfow for the high-blockage case when it continues to increase for the low blockage.

It has thus been exhibited that the blockage ratio has a key role on the way a laminar boundary-layer perturbated by single-scale hairpin street turns to become a turbulent-like boundary-layer.

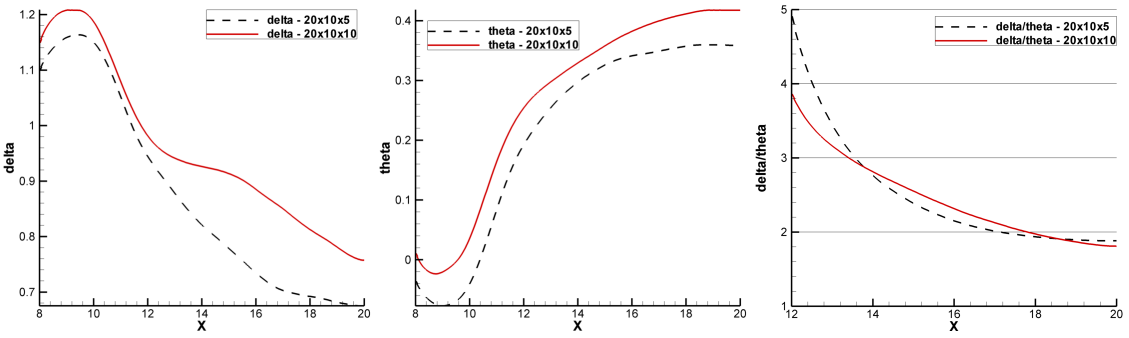


(a) (b) (c)

Figure 4.7: Evolution of $\delta$ (a), $\theta$ (b) and $\frac{\delta}{\theta}$ (c) for the high and low blockage grids in the median wake of the hemisphere

### 4.1.3 Comparaison of the autocorrelations and spatial intercorrelations: effect on the Strouhal number

#### Autocorrelations

The autocorrelations of the $u_1$ signal are compared for the probe $440$ which is located at the outlet, for $y = 2$ in the median plane. This points belongs to the path of hairpin heads in both cases. Figure 4.8 shows the associated plot. Both autocorrelations have been performed over $8000$ timesteps, with a constant length of $6000$ts for the time integration, and for a delay $\tau$ between $0$ and $2000$ts

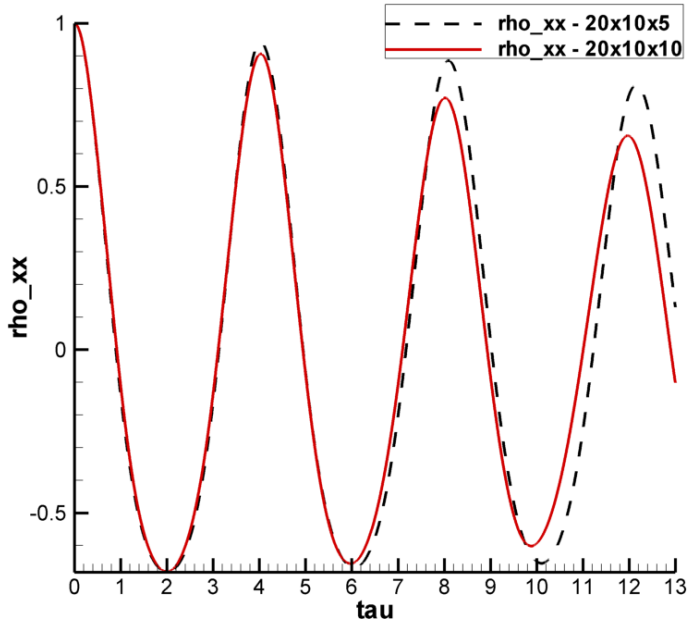


Figure 4.8: Autocorrelation of $u_1$ for a probe located at $x = 20$, $y = 2$ in the median plane for both low and high blockage grids

- Figure 4.8 shows that both signals are non-symmetrical as the anticorrelations are associated to lower levels than the correlations.
- The corelation levels are quite high with the three first peaks above $0.8$ for the high-blockage grid,

and above $0.65$ for the high-blockage grid.

- Figure 4.8 shows that the loss of correlation between two successive peaks is higher for the low blockage grid. It may either mean that there is a slight uncertainty on the period, that the convergence is less complete than for the high-blockage ratio, or that it can be assimilated to a behaviour closer to a turbulent flow than the high blockage grid.
- Although the first peak is fairly similar for both simulations, it appears from the second and third peaks that the period of oscillation is slightly lower for the $20 \times 10 \times 5$ case.

The Strouhal number is evaluated by measuring the time delay associated to the third correlation peak and dividing it by 3. The table 4.1.3 gives the values obtained for both cases: The error is quite low though

| | $20 \times 10 \times 5$ | $20 \times 10 \times 10$ |
|---|---|---|
| $St$ | 0.247 | 0.251 |

Table 4.2: Strouhal number comparaison for both simulations

considering that the timestep is $0.01$. The difference between the position of the first peak is only of 7 timesteps. However, this difference becomes more and more visible on the next peaks. As announced when looking at the snapshots, the shedding frequency is thus higher when the blockage is higher.

### Spatial intercorrelations

In order to evaluate the hairpin convection velocities, the intercorrelation of the $u_1$ signal between two consecutive probes is performed for both simulations: the probes, both in the median plane, are located respectively at $(x, y) = (18, 2)$ and $(x, y) = (20, 2)$. The figure 4.9 shows the intercorrelation signals for both grids The first peak is located almost exactly at the same position for both simulations. It leads to a

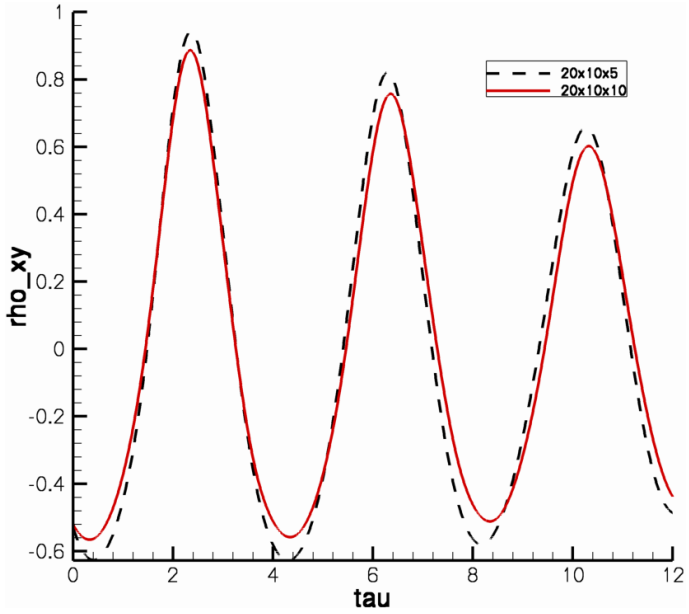


Figure 4.9: Intercorrelation of $u_1$ for two successive probes located at $(x, y) = (18, 2)$ and $(x, y) = (20, 2)$ in the median plane for both low and high blockage grids

convection velocity along the direction x of $0.85$, although given the fact that $y = 2$, we are over $\delta_{99}$. This velocity does not seem to be sensitive to the blockage ratio.

## 4.2 Effect of the height ratio $H$

The simulations 1 and 4 (table 2.1) are compared and will be refered as $20 \times 10 \times 5$ and $20 \times 10 \times 5H = 1.5$ respetively. The first one has an height ratio $H = 2$ while the second corresponds to a height ratio $H = 1.5$. The Reynolds number $Re_\tau$ is the same in both cases, and equal to 1000, but the Reynolds number $Re_\infty$ is respectively equal to 1348 and 1128 as the velocity on top of the sphere decrease with $H$.

### 4.2.1 Comparaison of the simulation statistics

### 4.2.2 Comparaison of the second order moments

Figure 4.10 shows the contours of $k$ in the median plane for both heigth ratios.

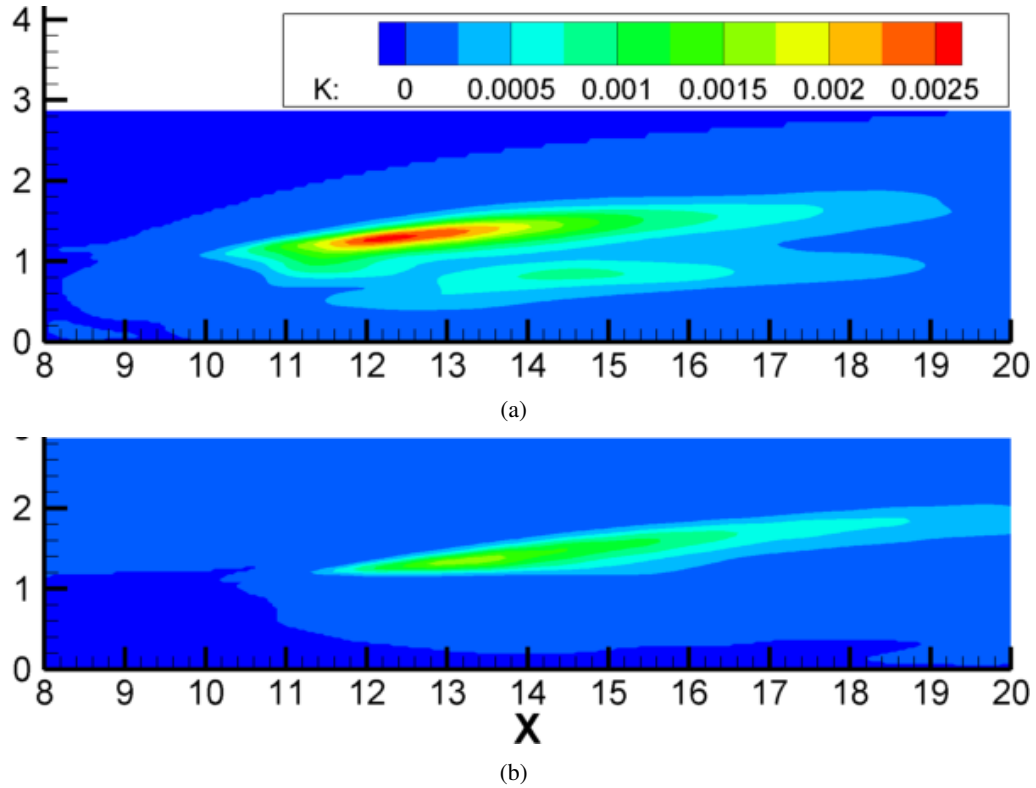


Figure 4.10: Contours of $k$ in the median plane for $20 \times 10 \times 5H = 1.5$ (a) and $20 \times 10 \times 5$ (b)

- It can be seen that $H = 1.5$ leads to higher values of $k$ as well as the presence of a second zone of maxima below the one associated to the hairpin heads.
- There is also an earlier shedding for the lower heigth ratio of at least an unit along the $x$ direction.

#### Comparaison of the boundary-layer associated statistics

Figure 4.11 shows the plot of the ratio $\delta/\theta$ for both simulations in the median wake of the flow. Figure 4.11 shows that the value in the all wake domain is lower for $H = 1.5$, meaning that if the aim was to provide a model of turbulent boundary-layer, the ratio would have to be set at $H = 1.5$ instead of $H = 2$. However, it will be seen in the next section of this chapter that the flow is far from being turbulent.

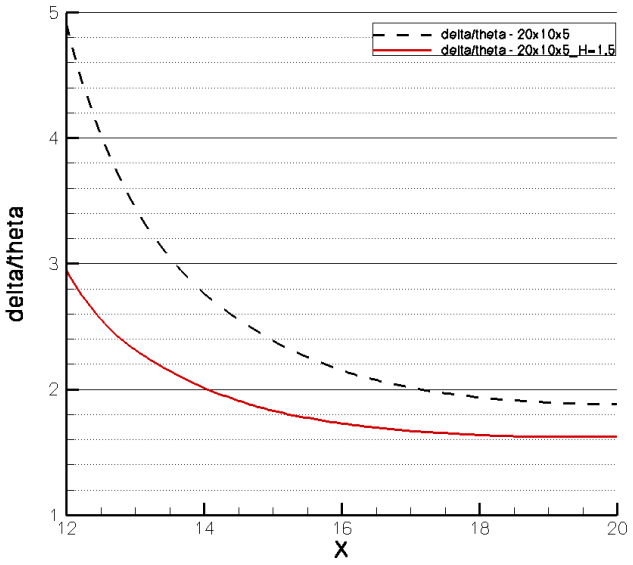


Figure 4.11: Comparaison of the ratio $\delta/\theta$ for both $H = 1.5$ and $H = 2$ heigth ratio in the median wake region

### 4.2.3 Comparaison of the autocorrelations

Like in the precedent section, autocorrelations of the $u_1$ signal are compared for the probe $440$ which is located at the outlet, for $y = 2$ in the median plane. This points belongs to the path of hairpin heads in both cases. Figure 4.12 shows the associated plot. Both autocorrelations have been performed over $8000$ timesteps, with a constant length of $6000$ts for the time integration, and for a delay $\tau$ between $0$ and $2000$ts

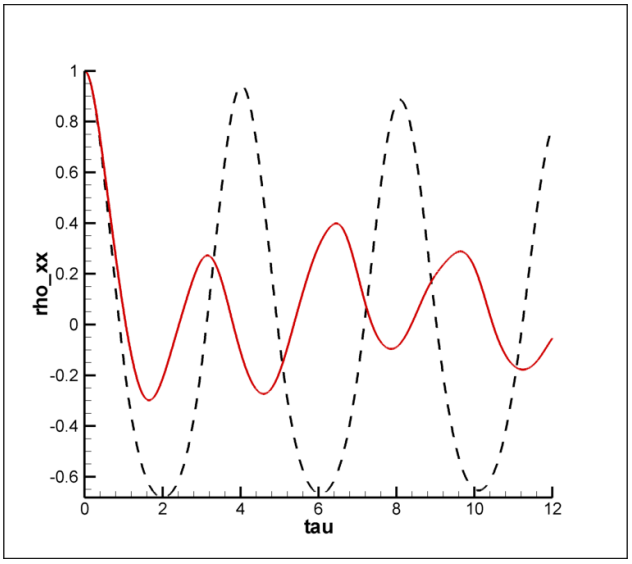


Figure 4.12: Autocorrelation of $u_1$ for a probe located at $x = 20$, $y = 2$ in the median plane for both low and high blockage grids

- The level of correlations are strongly lower for the $H = 1.5$ case. It may indicate that the flow is less periodical, especially by considering that the levels of coherence of the secondary peaks are not, as it was for both the $20 \times 10 \times 5$ and $20 \times 10 \times 10$ cases, decreasing linearly

- However, it also has to be pointed out that only $10000$ iterations have been performed for this case, instead of more than $20000$ for the $20\times10\times5$ case. It may be the effect of an incomplete convergence.
- It can also be seen that a change diminution of $H$ leads to a strong increase of the Strouhal number to $0.31$, which means about $17\%$ of variation compared to the $20 \times 10 \times 5$ case.

## 4.3 Study of different statistics for the $20 \times 10 \times 5$ simulation

The idea of this short section is to study the statistics and associated autocorrelations of some quantities that can be made of the acceleration and velocity field in order to get some insight in eventual ways to detect the hairpins as well as the way the acceleration and velocity field interact. The study will only be performed using the results of the probe $440$ which is located at the outlet, on the median plane, at $(x, y, z) = (20, 2, 2.5)$. Figure 4.15 shows the fluctuating parts of the two non-zero components of the velocity field $u_1'$ and $u_2'$, the two non-zero components of the acceleration field $a_1'$ and $a_2'$, as well as $\mathbf{a}'.\mathbf{u}'$ and $(\mathbf{a}'\times\mathbf{u}')_3$ (which is the only non-zero component of the cross product as both velocities and acceleration have a zero component along the $z$ direction in the median plane).

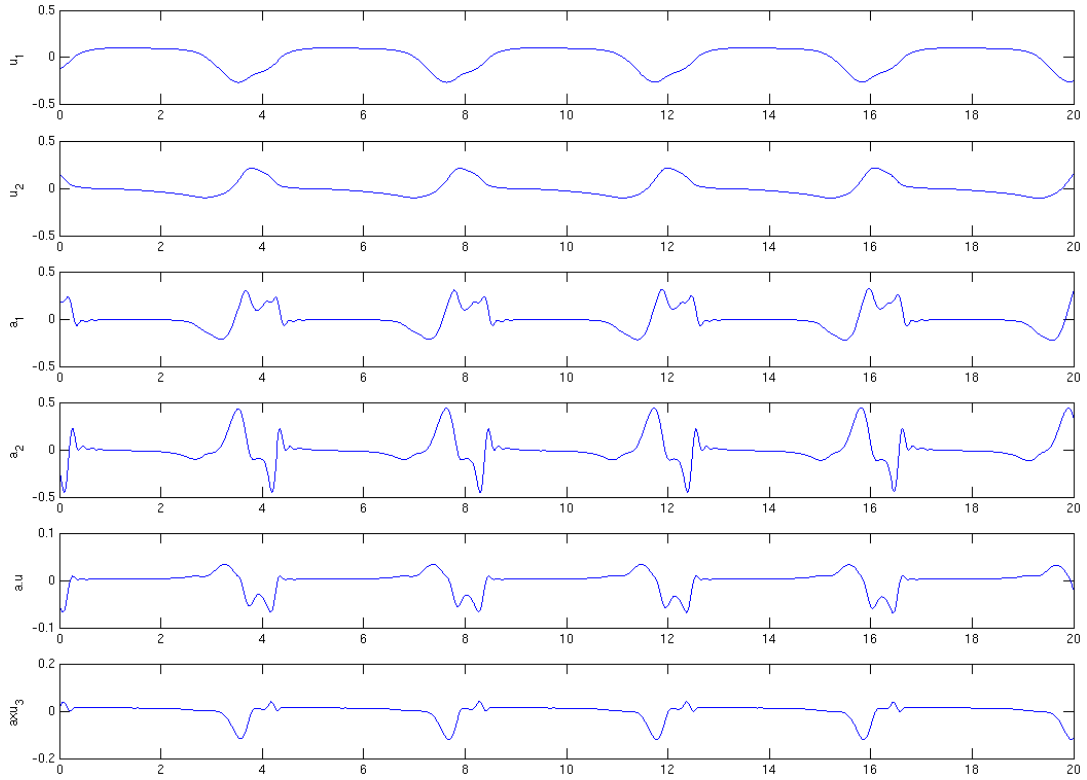


Figure 4.13: Plot of $u_1'$, $u_2'$, $a_1'$, $a_2'$, $\mathbf{a}'.\mathbf{u}'$ and $(\mathbf{a}'\times\mathbf{u}')_3$ against $t$ for the probe located at $(x, y, z) = (20, 2, 2.5)$

- First of all, figure 4.15 shows that all the plotted components are highly periodical, though one can wonder to what point this is influenced by the fact that the probe is located at the outlet, meaning that the flow is simply convected here. It thus seems to prove that the acceleration, and thus the associated forces using the Newton's principle, are correlated in time.
- Secondly, it can be seen that the all the signals show a clear pattern allowing to locate the moment where the hairpin passes through
- It is easier to locate this interval on the acceleration or $\mathbf{a}'.\mathbf{u}'$ and $(\mathbf{a}' \times \mathbf{u}')_3$ signals than using the velocity signal as the variation is stronger than for the velocity signals. For instance, $(\mathbf{a}' \times \mathbf{u}')_3$

is always positive except when the hairpin passes through. This behaviour should be confirmed by plotting the same kind of signals for other probes, but it may be a really efficient way to detect hairpins.

- When comparing the signals $u_1$ and $u_2$, it can be seen that the first one is minimal for an hairpin while the second one is maximal. Given that the hairpins heads rotate anti-clockwise along the crossstream direction, it means that the probe is located above the line of hairpin heads center (there is a $u_1$ minimum on top of the hairpin, and a $u_1$ maximum below).
- It can also be seen that $u_1$ and $a_1$ recover faster a constant value than $u_2$ and $a_2$, showing that the time of influence of an hairpin is longer along the $y$ direction than along the $x$ direction, which may come from the fact that $x$ is the direction of the mean flow.

Finally, figure 4.14 shows the associated autocorrelations for the 6 signals considered: To measure the level

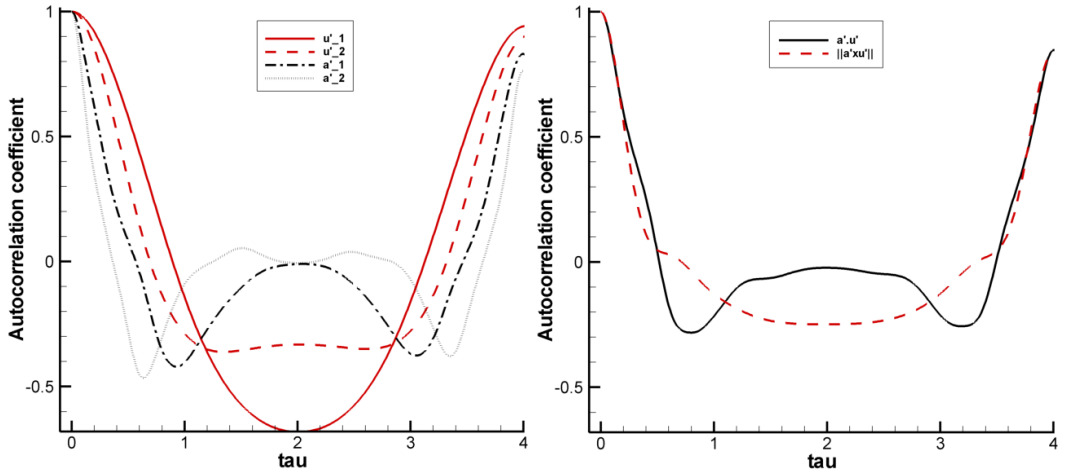


(a) (b)

Figure 4.14: Autocorrelation of $u_1'$, $u_2'$, $a_1'$, $a_2'$ (a), $\mathbf{a}'.\mathbf{u}'$ and $(\mathbf{a}' \times \mathbf{u}')_3$ (b) for the probe located at $(x, y, z) = (20, 2, 2.5)$

of corerlation of these different signals, the integral scale are evaluated:

$$L_T(x) = \int_0^{\infty} \rho_{xx}(\tau) d\tau \tag{4.1}$$

However, in our case, the length of the considered signals are not sufficient to get a convergence towards zero, this value is evaluated over three periods as it is the biggest multiple of the period for the autocorrelation time available:

$$L_T(x) = \int_0^{\frac{3}{St}} \rho_{xx}(\tau) d\tau \tag{4.2}$$

Using the Strouhal number given in table 4.1.3, the values of $L_T$ for $u_1'$, $u_2'$, $a_1'$, $a_2'$ (a), $\mathbf{a}'.\mathbf{u}'$ and $(\mathbf{a}' \times \mathbf{u}')_3$ are given in table 4.3 It thus seem that the only quantity geting a positive integral scale is $\mathbf{a}'.\mathbf{u}'$. The other

| $u_1'$ | $u_2'$ | $a_1'$ | $a_2'$ | $\mathbf{a}'.\mathbf{u}'$ | $(\mathbf{a}' \times \mathbf{u}')_3$ |
|---|---|---|---|---|---|
| $-0.0585$ | $-0.0547$ | $-0.0324$ | $-0.0087$ | $0.4487$ | $-0.0314$ |

Table 4.3: Integral scales over 3 periods of the autocorrelation signals of $u_1'$, $u_2'$, $a_1'$, $a_2'$ (a), $\mathbf{a}'.\mathbf{u}'$ and $(\mathbf{a}' \times \mathbf{u}')_3$

signals, though getting high positive correlation peak levels, are associated for most of the delays over a period with a negative correlation levels.

## 4.4 Validation of the recycled condition

In order to validate the method of recycled condition, the plots of $\delta/\theta$ are compared for $x = 12$ to $x = 20$ in the median line for both the $20\times10\times5$ domain and the recycled domain in figure **??** The two plot are exactly

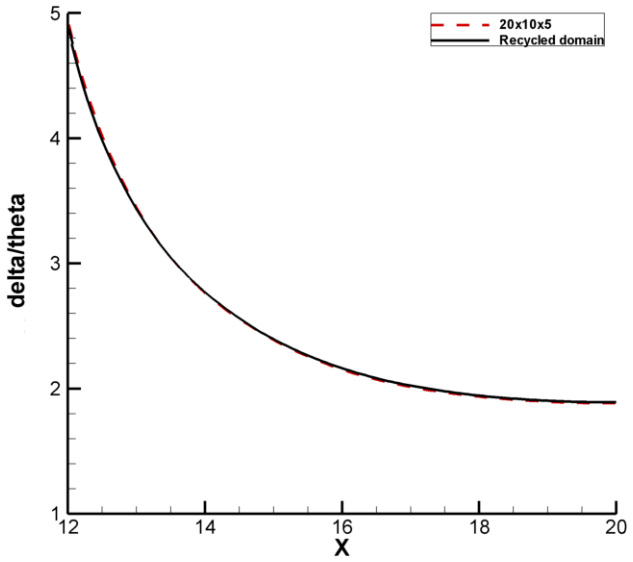


Figure 4.15: Comparaison of the plots of $\frac{\delta}{\theta}$ against $x$ for $x = 12$ to $x = 20$ in the median line for both the $20 \times 10 \times 5$ domain and the recycled domain

equal, and thus the recycled condition will be used with full confidence to test the plasma actuators. A more rigourous validation has been performed by [12] who has compared after an high number of iterations two instantaneous isosurfaces of vorticity for the complete domain and the recyled domain and shown that they were exactely equal.

# Chapter 5

# Defintion and use of the critical point theory and the Q-criterion isosurfaces to explore the physics of Hairpin flows

## 5.1 Introduction

The aim of this chapter is to get more insight into the physics of the hairpins. Using the unsteady fields of velocity and accleration, the topology of the flow will be investigated. Many studies of that kind have already been performed on two-dimensional fields, like [16], and the simple and unperturbated structure of a single hairpin or an hairpin streets make it an ideal case to try to apply such theories to a three-dimensional flow. The idea will be to try to investigate the nature of the core lines of the hairpins and the presence of non-zero divergence points on the acceleration fields, which are points for which a volumic force is applied as the work of the acceleration is non-zero. First of all, the link between the Lagrangian acceleration field and the Q-criterion is investigated.

## 5.2 Link between the Lagrangian acceleration field and the Q-criterion is investigated

By definition, the Lagrangian acceleration field is equal to:

$$\mathbf{a} = \frac{D\mathbf{u}}{Dt} = \frac{\partial \mathbf{u}}{\partial t} + \mathbf{u}.\nabla\mathbf{u} \tag{5.1}$$

The Q criterion is defined as the difference between the rate-of-rotation and the rate-of-strain of the Jacobian matrix of the velocity field.

$$Q = \frac{1}{2}\left(||\Omega||^2 - ||S||^2\right) \tag{5.2}$$

It has also been proven to be proportional to the laplacian of the pressure field. It is one of the most efficient criterions to detect coherent structures, as the core of this latters is usually a zone of low pressure. When the rate-of-rotation becomes dominant compared to the rate of strain, which corresponds to positive values of the Q-criterion, it means that we are inside a coherent structure. The main interest of the $Q - criterion$ compared to the study of the vorticity fields is that it is not triggered by a simple shear and thus is not trigerred at the walls. In these zones, there is usually vorticity because of this strain, but not necessarely coherent structures. One of the definition of the Q-criterion is:

$$Q = -\frac{1}{2}u_{i,j}u_{j,i} \qquad \text{where} \qquad u_{i,j} = \frac{\partial u_i}{\partial x_j} \tag{5.3}$$

Then, using the equations 5.1 and 5.3:

$$\begin{aligned}
\nabla.\mathbf{a} &= \frac{\partial}{\partial x}\left(\frac{\partial u_1}{\partial t}+u_i\frac{\partial u_1}{\partial x_i}\right)+\frac{\partial}{\partial y}\left(\frac{\partial u_2}{\partial t}+u_i\frac{\partial u_2}{\partial x_i}\right)+\frac{\partial}{\partial z}\left(\frac{\partial u_3}{\partial t}+u_i\frac{\partial u_3}{\partial x_i}\right)\\
&= \frac{\partial}{\partial t}\left(\underbrace{\nabla.\mathbf{u}}_{=0}\right)+u_1\frac{\partial}{\partial x}\left(\underbrace{\nabla.\mathbf{u}}_{=0}\right)+u_2\frac{\partial}{\partial y}\left(\underbrace{\nabla.\mathbf{u}}_{=0}\right)+u_3\frac{\partial}{\partial z}\left(\underbrace{\nabla.\mathbf{u}}_{=0}\right)\\
&\quad +\left(\frac{\partial u_1}{\partial x}\right)^2+\left(\frac{\partial u_2}{\partial y}\right)^2+\left(\frac{\partial u_3}{\partial z}\right)^2+2\frac{\partial u_2}{\partial x}\frac{\partial u_1}{\partial y}+2\frac{\partial u_3}{\partial x}\frac{\partial u_1}{\partial z}+2\frac{\partial u_3}{\partial y}\frac{\partial u_2}{\partial z}\\
&= u_{i,j}uj,i\\
&= -\frac{1}{2}Q
\end{aligned}$$

Thus, as a conclusion, the following relation links the Q-criterion and the Lagrangian acceleration field:

$$\nabla.\mathbf{a} = -\frac{1}{2}Q \tag{5.4}$$

The idea now is to use this relation to investigate the flow field. As the cores of the structures are supposed to be the zone where $Q$ is maximal, the acceleration field can be investigated. Moreover, the star-critical point of the acceleration field cannot be found using the classical critical point theory on the velocity field, as this latter is bound to get a zero-divergence due to the incompressibility equation. The idea will thus be to use the tools defined by [16] and [2] on other fields than the velocity field to investigate the unsteady field provided by our simulation. The aim is also to try to find a criterion without treshold, as the analysis of Q criterion and of the shape of coherent structures highly depends on the value used to define these isosurfaces.

## 5.3 Search for the hairpin core lines

The first idea was to try to find the local maximums and minimums of the Q field. The first way to do so was to evaluate locally the components of the Q-criterion gradient using first order finite-differences and to spot all the points for which sign changes were occuring for at least two of the gradients components. This method gave too many points. The second problem of such a method is that the extremums are only searched on the nodes of the mesh, and there is no physical reason for this nodes to coincide with the structures. Moreover, using first order finite difference approximations of the gradients components was unapropriate given the fact that the code provides efficient algorithm to evaluate the derivatives, using $6-th$ order compact schemes which are far more accurate. Finally, the fact that a point is an extremum along two directions is not sufficient enough to get a local extremum. It could, for instance, be a saddle point in one of the referential planes and an extremum in another one. It led to the conclusion that more directions had to be investigated.

To avoid the problem of localisation at the nodes, a new method has been tested:

1. First, the Q gradients are evaluated on the mesh
2. Then, for each node of the mesh, the presence of a zero along the line linking it to a neighbouring node is investigated for the three components.
3. If for a given direction, at least two components of the Q gradient change between the two nodes, the position of this zero is extracted for each component by linear interpolation along the direction
4. Then, the actual position of the zero is obtained by averaging the positions of the zeros for each components. All these zeros are in the line between the two nodes, and thus the average is also on this line.

This new process is better than the first one as it gives already some liberties concerning the position of the zero (not necessarely a point of the mesh), and also because it leads to the investigation of more directions.

Even if this method is not foolproof, we could see by having a look at some slice planes that at least two components of the Q-gradient were changing their signs between both sides of a core line. But plotting all the local extremum for which $Q$ is positive leads once more to two many points. To find a kind of cutting value with physical meaning, the PDF of the $Q$ value in all the edges considered has been compared to the PDF of the local extremums and can be seen in figure 5.1 It can be seen in fig. 5.1 that the pdf of the

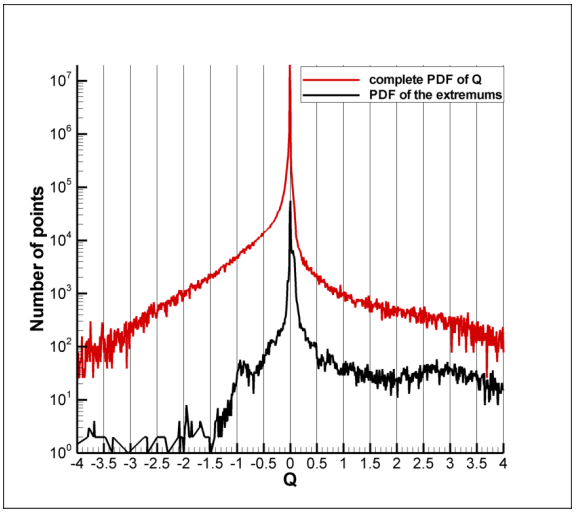


Figure 5.1: PDF of Q for all the edges considered by the method compared to the PDF of Q for all the points selected as extremums by the method

extremums exhibit a cutting value at $Q = 0.5$ above which the curve follows a constant slope. This value of $0.5$ is a threshold, but with a somewhat physical meaning. Figure 5.2 shows the isosurface of $Q = 1.5$ for the $20 \times 10 \times 5$ simulation at a given instant. The red spheres are maximum associated with values $Q > 1$, the yellow ones for $0.5 < Q < 1$, the blue ones for $Q < -1$ while the light blue ones are associated with $-1 < Q < -0.5$. The structure of the hairpins is well rendered even though too many points are considered. Local filtering and tracking methods towards the extrema may be added to the method to increase the level of selection. The second big flaw of this method is that the physical meaning of these extremums is not known, and it will thus be hard to extract information appart from the position of the core lines.

## 5.4 Perspectives

Some procedures have been tested using the critical point theory, based on the obtention of the deformation matrix of $\mathbf{grad}Q$, but without success for now. Only 2D extremum points are found efficiently. This method will have to be implemented on the framework of $3D$ critical point theory to find the nature of critical points in the eigenvector planes.

Figure 5.2: Isosurfaces of $Q$ and extremums detected by the extrema algorithm for a $20 \times 10 \times 5$ simulation instantaneous velocity field

# Chapter 6

# First results in Plasma forcing

## 6.1 Plasma Actuators and their numerical Implementation

The aim of this study was to run numerical simulations of plasma actuators on a simple hairpin street. The final objective is to reduce the associated skin friction on the wall. Yet because of lack of time, this part of the study has not been granted with the time it would have been needed to get really pertinent results and the insight we were looking for on this kind of actuators. It has not been possible either to try to match experimental or numerical results provided for instance in [6], [15] or [3]. Firstly, simple numerical simulations without any flow will be performed to test the actuator model and its associated parameters. Then, once everything is set up, some simulations will be run on the hairpin flow. But first of all, the principle of plasma actuators has to be explained. It has been used for the last ten years in aeronautics, for instance for leading-edge separation control on airfoils as in [15]. [6] have described experimentaly three plasma actuators without any flow: the DC (Direct Current), DBD (Dielectric Barrier Discharge) and the sliding discharge actuator. Only the DBD actuator will be modeled and studied here. Figure 6.1.(a) gives a sketch of the DBD actuator extracted from [6] The principle of the Direct Barrier Discharge is to get one

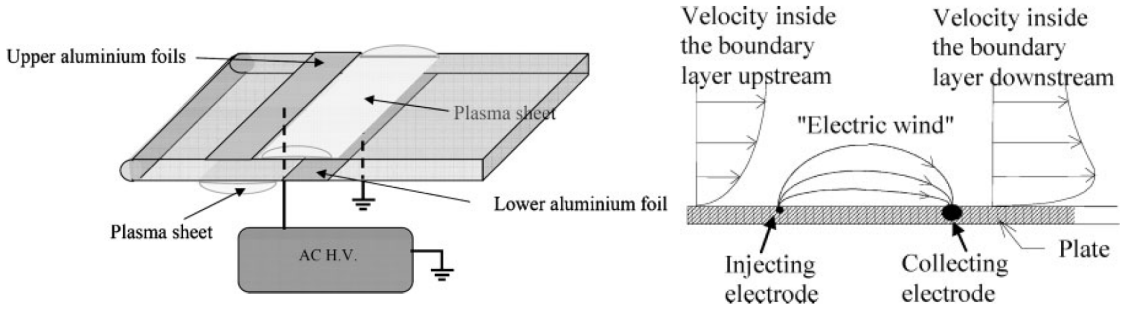


(a) (b)

Figure 6.1: sketches of the DBD plasma actuator (a) and of the plasma actuator principle (b) extracted from [6]

of the two immerged at the surface of the flow while the second one is immerged into a dielectric material. The difference of potential between these two electrodes generate an ionised gas at the positive electrode, and those ions are then attracted by the negative electrode, generating an artificial wind that will be used for control purpose. Figure 6.1.(b) shows the principle: the collecting electrode, negatively charged, will attract the ions created at the injecting electrode.

One of the major interests of the plasma actuators is that it is one of the only actuators which is completely non-intrusive, generating the effect asked without creating blockage or vorticity like for instance flaps or jets. It is however, at least for now, only partially understood and mastered experimentally or numerically.

And for instance, the repartition of the ions and the way the electrical field generated can be converted into a forcing field, the net charge density, is badly understood. Yet [21] provide a numerical model avoiding the need of this net charge density. The approach for our simulations will rather simple: the net charge density is set equal to 1 everywhere. The aim of this net charge density function is to provide a minimum level of $\mathbf{E}$ for which ionisation occurs. Thus, in the present case, it will occur everywhere, even though the electrical field decrease rather fastly. Both electrodes are set to a potential of $-1$ and $+1$. The norm of $\mathbf{E}$ is controled by a proportionality factor. The forcing field is then injected into the Navier Stokes equations and its contribution to the flow is evaluated at the same time as the contribution of obstacles using a direct forcing method described briefly in chapter 2.

Figure 6.2 shows the the wind generated experimentally by a single DBD actuator extracted from [6] Figure 6.2 shows that the length of penetration, which is defined by the heigth of the $u_1$ maximum generated

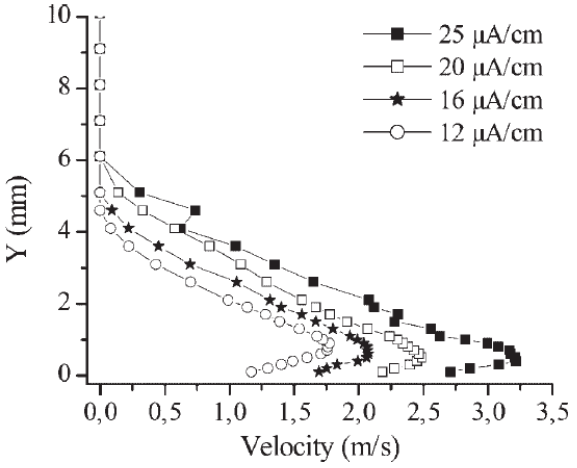


Figure 6.2: Wind generated experimentally by a single DBD actuator extracted from [6]

by the actuator, does not depend on the applied current but only in the actuator geometry, as quoted for the quite similar situation of electromagnetic forcing by [14].

## 6.2 Simple case of 2D forcing

### 6.2.1 Forcing in a box

The first step is going to be to apply the forcing without a velocity field. The domain is set to $L_x = 10$, $L_y = 10$, $L_z = 0.2$ for an almost $2D$ simulation. In order to keep the same resolution in the $x$ and $y$ directions as for the hairpin simulations, $n_x = 181$ and $n_y = 121$. $n_z$ is set to 4. All the boundaries are considered as wall in both the $x$ and $y$ directions. The $z$ direction remains periodic. The plasma actuator is made 2D by setting up a succession of consecutive actuators along the $z$ direction. The effect is to generate a zero-value $E_3$. The forcing field is considered as applied continuously to the same steady value. The increase in $\|\mathbf{E}\|$ generated by the add of several electrodes to generate the 2D field is controlled by a proportionality constant applied to the field to get the same norm as it would be found for a unique actuator. The width of the electrodes is set to $10\Delta_x$. The ratio between this width and the other geometric parameters defined in [6] is conserved, leading to an electrode length of $40\Delta_x$, a gap of $10\Delta_x$ between the two electrodes, and the second electrode located $2\Delta_x$ deep in the ground. Figure 6.3 shows the $u_1$ field as well as some vectors along $x =$const. profiles close to the electrodes. It shows that a wind is generated on top of the collecting electrode while a blockage is generated on top of the injecting electrode, generating reverse flow along the $x$ direction. Profiles at $x = 3.5$ and $x = 4$ also show a pumping towards the electrode on the $y$ direction which is the proof of a large-scale effect of the actuator. The actuator seems to get the correct behaviour. Yet the change of signs of the $u_1$ component further above the collecting electrode for $x = 5$ seems to show

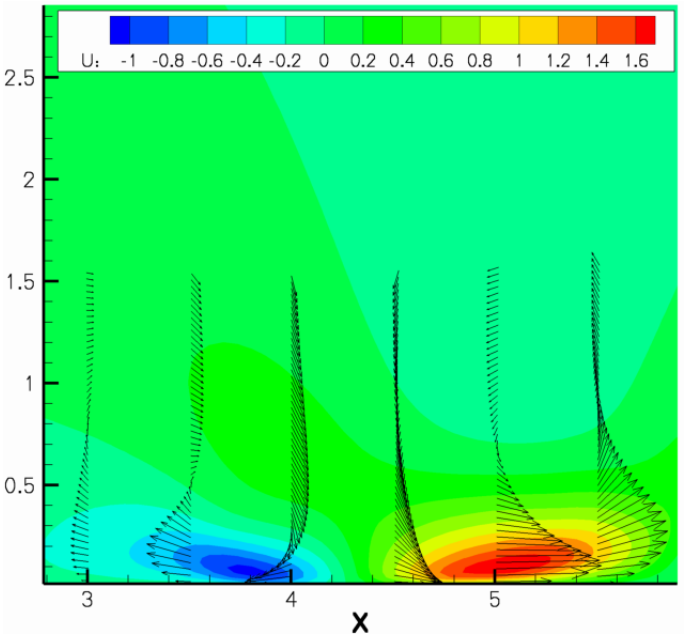


Figure 6.3: $u_1$ field as well as some vectors along $x$ =const. profiles close to the electrodes for a $2D$ actuator on a closed $2D$ box without incoming flow.

the presence of a vortex generated along the electrode which is not coherent with the results provided by [21] who have done the same kind of simulation on a DBD actuator, but using a net density modelisation. It will be seen on the 3D actuator that this problem leads to undesired structures. However, knowing its flaws, this model will be kept for the following experiments

### 6.2.2 Forcing of a Blasius boundary-layer

In order to get closer from the 3D situation of plasma forcing on hairpin vortices, the same domain is used, but with an incoming boundary layer of heigth ratio 2 (compared this time to the non-dimensional reference length which is set to 1 even though there is no hemisphere in that case). The top boundary is set to a no-slip condition, while a convective equation for the velocity field is applied at the outlet. Figure 6.4 shows the resulting mean $U_1$ contours as well as mean streamlines. The electrodes are centered at $x = 4.5$ It can be

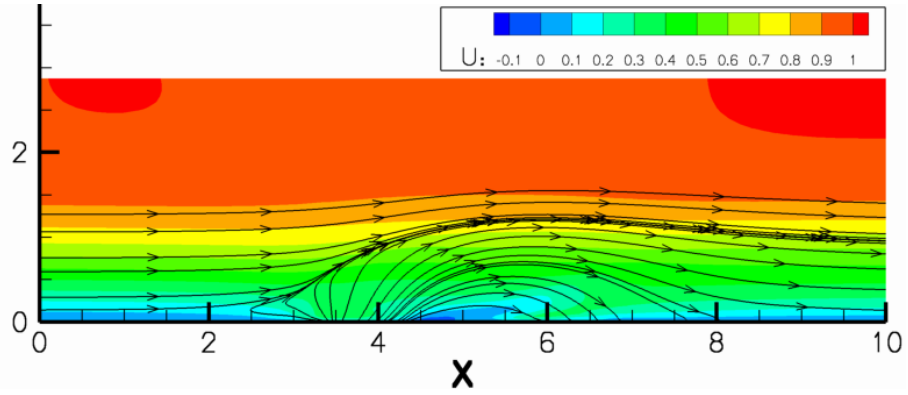


Figure 6.4: mean $U_1$ contours as well as mean streamlines for the forcing of a Blasius boundary-layer

seen that the blockage effect generated close to the injecting electrode generates a separation of the flow, and the pumping towards the electrode can also be noticed close to the positive electrode, even though the blockage effect generates a deviation towards the top of the streamlines. There is no structure creation further above the electrodes as it occured in 2D, but one can consider that such a structure would be flushed as it would be generated around the cross-stream direction.

## 6.3 First try of 3D forcing

### 6.3.1 Domain used

The idea is now to apply the actuator to a fully 3D field. The recycled condition presented in chapter 2 is used at the inlet, and the flow downstream the plane of capture at $x = 12$ is used as an initial condition. Figure 6.5 shows both the plane and a visualisation of the initial flow using isosurfaces of $Q$ for a threshold level of $1.5$.

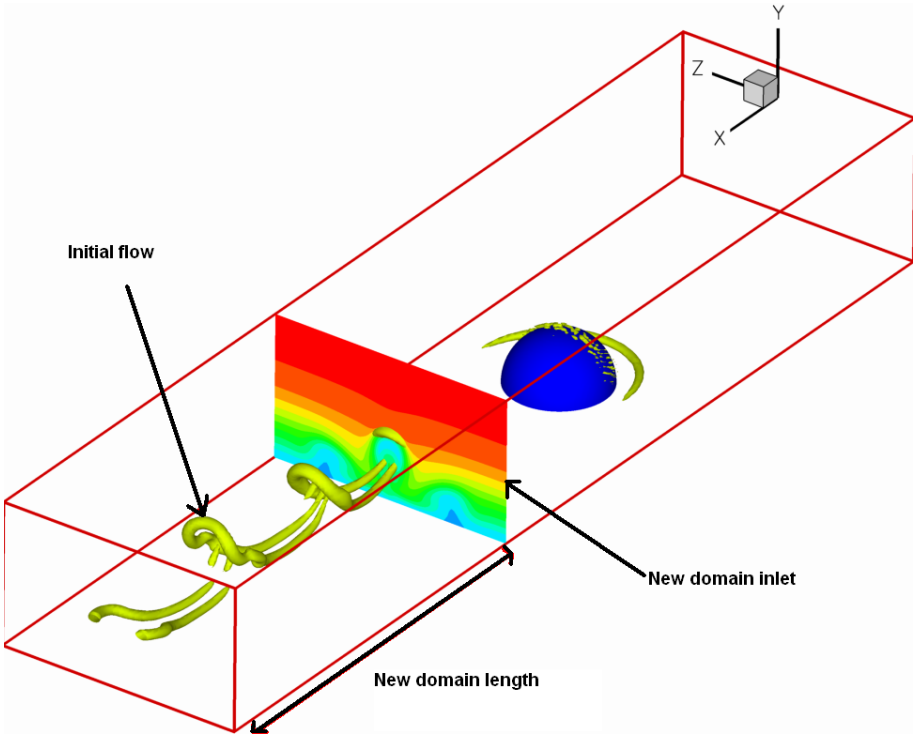


Figure 6.5: Representation of the new domain used for hairpin forcing

### 6.3.2 Position of the actuators

The idea here was to act on the legs of the hairpins which are the closest to the floor. The electrodes are located along the $x$ axis this time in order to try to flush the legs away. In order to generate a maximum upflow on the median plane to counter the downflow generated by the hairpins, two actuators are located in both sides of the median plane, at equal distance. Both the positive electrodes are located on the median plane side. The electrodes are centered in the $x$ direction at $x = 2$. Figure 6.6.(a) shows an unsteady velocity field in a $x = 4$ plane of $\|u\|$ as well as the streamlines of the flow in this plane while figure 6.6.(b) shows the contours of $\|\mathbf{E}\|$ as well as the streamlines of $\mathbf{E}$ in the same plane. At this $x - value$, the $E_3$ field is equal to zero. The field generated is thus thinked to be as opposite as possible to the streamlines generated by th legs in order to perturbate them and thus perturbate their effect on the skin friction.

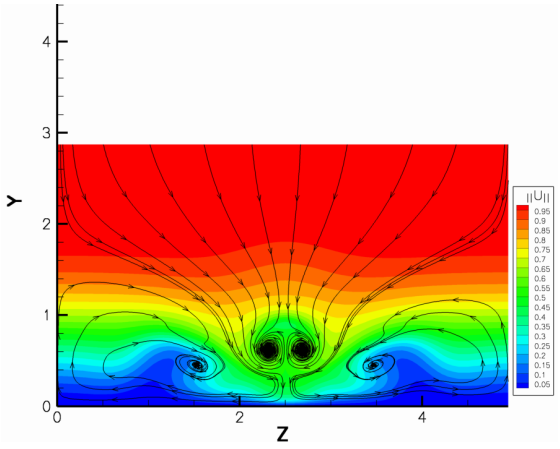


(a)

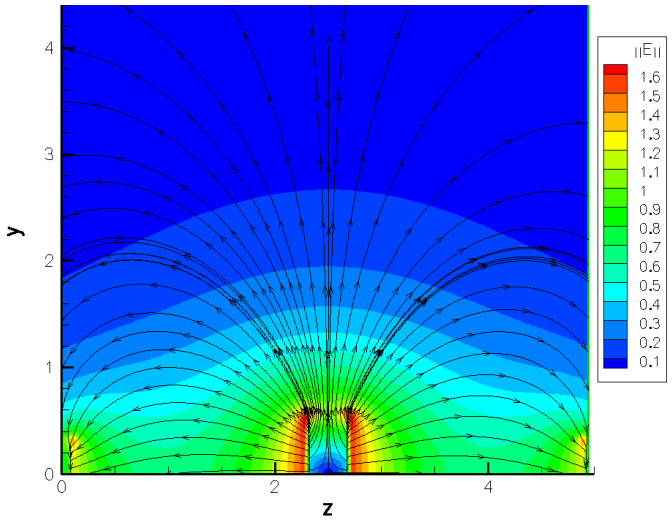


(b)

Figure 6.6: streamlines and contours of $\|u\|$ of the flow without forcing (a) and contours of $\|\mathbf{E}\|$ as well as streamlines of $\mathbf{E}$ (b) in the plane $x = 4$

### 6.3.3 First results

The simulation is runned with and without forcing. After approximately 3000 iterations to ensure the convergence of the plasma actuator effect on the flow, two snapshots are taken using isosurfaces of $Q$ with a threshold level of 1.5, and colored by the $u_3$ velocity.

#### Snapshots

Figure 6.7 shows these two snapshots.

- It can be seen that the hairpins are perturbated by the forcing, but not enough to loose their structures. However, they are slightly swept away along the $z$ direction, even though the idea was to separate them
- One can also notice in fig. 6.7.(b) the presence of secondary structures generated above the electrodes. Unlike the boundary layer case, these structures are generated along the stream direction and thus are not flushed by the flow.

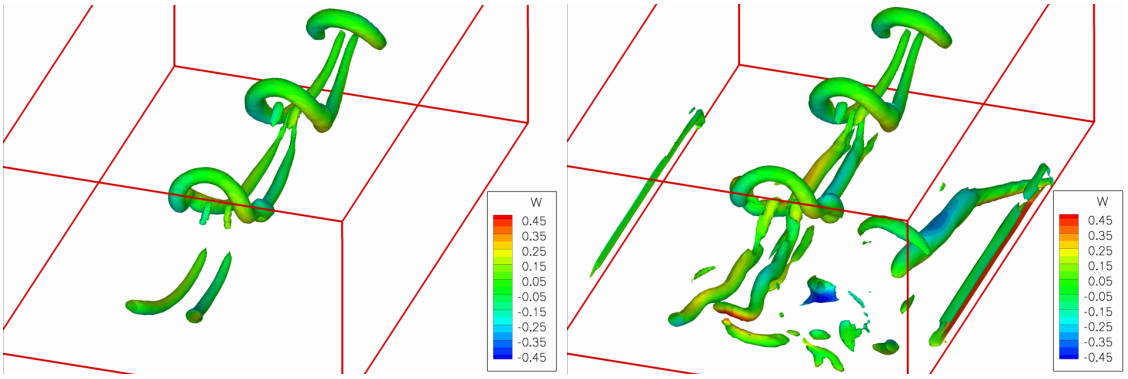


(a) (b)

Figure 6.7: Snapshots of the $Q$ criterion isosurface with a threshold level of $1.5$, and colored by the $u_3$ velocity with (b) and without (a) plasma after $3000$ timesteps

- These structures also have the big disavantage of being generated close to the periodic condition borders. The electrical field provided may not be periodic enough along the direction $z$

Even though non desired secondary structures are generated, the drag integrated over the all floor for both simulations is compared in figure 6.8 It shows that the forcing has a drag reduction effect which remains to

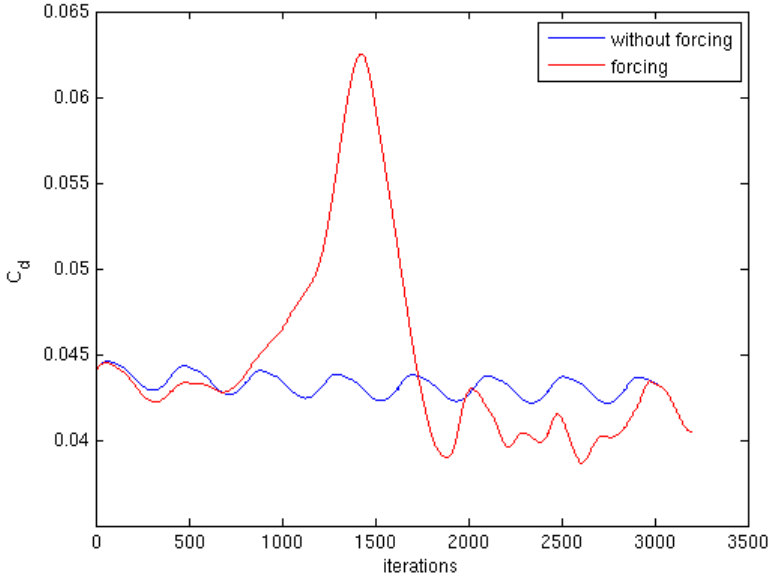


Figure 6.8: Comparaison of the drag coefficient integrated over the whole floor against time both with and without forcing

be confirmed by evaluation of the mean flow. The peak in figure 6.8 for the forcing curve is supposed to be related to the convergence of the plasma actuator and should not occur anymore for the next timesteps.

But given th flush along the $z$ direction constated on the snapshots of figure 6.7, the loss of drag could generate an increase in skin friction along the $z$ direction. Figure 6.9 compares both $w_\tau$ fields at the same instant where the snapshots have been taken. Figure 6.9 shows, as predicted, a strong increase of $w_\tau$ close to the periodicity condition. The control process proposed has thus only redistributed the skin friction along the $z$ direction, and the cut in the drag noticed in figure 6.8 should be the conequence of it.

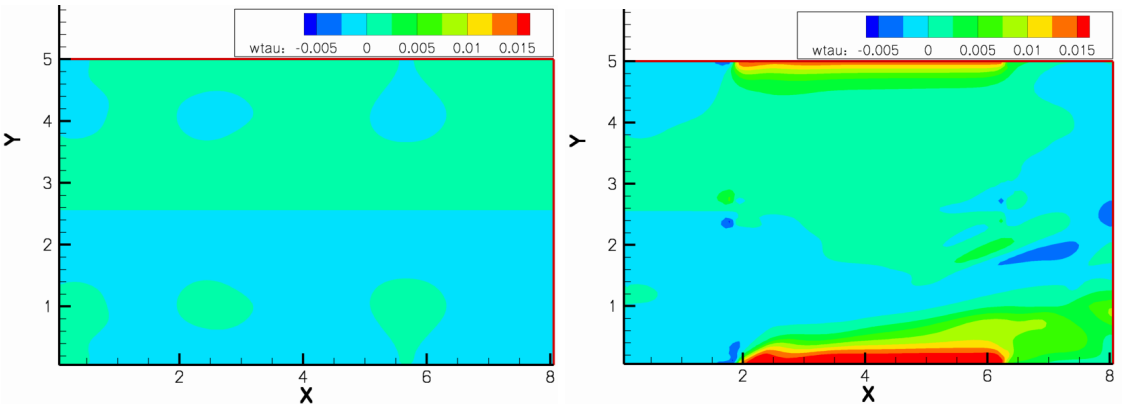


(a) (b)

Figure 6.9: $w_\tau$ fields on the floor both with (b) and without (a) plasma after 3000 timesteps

The next step for this plasma study will be to try the same actuators using a recycled condition for the wider domain to see how the periodicity condition affects the flow. Another problem is that the size of the actuators is close to the size of the structures, and it is not usually reckoned as the best way to control a flow. Work will have to be done on the model to be able to generate more large-scale effects with smaller actuators. However, this first results show that controlling hairpins with plasma actuators is possible, even at high heigth ratios $H$ for which the structures generated are far from the surface and moving away from it.

# Chapter 7

# Conclusion

Direct Numerical Simulations have been performed for the generation of hairpin streets by perturbating an initially laminar boundary layer by an hemisphere, and it has been shown to be a good method to general regular hairpin streets. This framework good both to test plasma actuators and dectection criteria as it is a simple laminar flow with only few characteristic length scales associated to the hairpins.

The effect of some parameters like the blockage or the heigth ratio have been characterized on the flow statistics as well as its ability to generate a turbulent-like model of boundary-layer. However, the effect of other parameters like the Reynolds number have to be characterised also. It has not been possible here both by lack of time and by the difficulty by the code to become unstable for lower Reynolds number given the high aspect ratio considered ($H = 2$). In [1] and [9], the heigth ratio are lower, certainly explaining why they get the shedding easier. A second effect woul be to consider the fact that the mesh used was defined for $Re_\tau = 1000$, and may be too refined for lower Reynolds numbers. Even though there i no such thing as too fine grid, it may lead the unstablility to take far more time to reach the sufficient level to lead to a shedding.

Some detection criteria have also been tested, especially using critical point theory. But they have failed to give us the physical points of the flow and only them, leading to a need of threshold level which make these methods unefficient for a systematic use. However, some successes have been obtained in 2D planes and will have to be adapted to the study of the flow in the planes normal to the eigenvectors associated to the deformation matrices. An extremum criteria has also been created, leading to a quite good detection of the vortex core, though it will have to be enhanced, using local filters for instance.

As far as plasma forcing is considered, a simple model has been tested but is not accurate enough to match experimental results even in $2D$. One of its main flaws is the creation of vortices on top of the electrodes, which may come frome the fact that the net charge density is set to 1 everywhere. It has led to a diminution of the skin friction along the $x$ direction of the hairpins, but has also generated an increase in the $z$ direction. However, it shows that controlling hairpins with plasma is possible, and the use of a wider domain should remove some of the problems encountered.

# List of Figures

# List of Tables

# Bibliography


[1] M.S ACARLAR and C.R. SMITH. A study of hairpin vortices in a laminar boundary-layer. part 1. hairpin vortices generated by a hemisphere protuberance. *Journal of Fluid Mechanics*, 175:141, 1987.

[2] M.S. CHONG A.E. PERRY and B.J. CANTWELL. A general classification of three-dimensional flow fields. *Physics of Fluids*, 2-5, 1990.

[3] C.L. ENLOE G.I. FONT J. RONEY C.O. PORTER, T.E. McLAUGHLIN and B.W. BAUGHN. Control using a dbd plasma actuator. *AIAA*, 786, 2007.

[4] G.S. CONSTANTINESCU and K.D. SQUIRES. Les and des investigations of turbulent flow over a sphere at re = 10,000. *Flow, Turbulence and Combustion*, 70:267–298, 2003.

[5] M. DEVLIN. *Dynamic wings*.

[6] G. ARTANA M. FORTE G. TOUCHARD E. MOREAU, C. LOUSTE. Contribution of plasma control technology for aerodynamic applications. *Plasma Process. Polym.*, 3:697707, 2006.

[7] P. ORLANDI E.A. FADLUN, R. VERIZICCO and J. MOHD-YUSOF. Combined immersed-boundary finite-difference methods for three-dimensional complex flow simulations. *Journal of Computational Physics*, 161:3560, 2000.

[8] A.H. HAIDARIT and C.R. SMITH. The generation and regeneration of single hairpin vortices. *Journal of Fluid Mechanics*, 211:135–162, 1994.

[9] M.E. PAPKA H.M. TUFO, P.F. FISCHER and M. SZYMANSKI. Hairpin vortex formation.. a case study for unsteady visualization. 1999.

[10] T.A. JOHNSON and V.C. PATEL. Flow past a sphere up to a reynolds number of 300. *Journal of Fluid Mechanics*, 378:19–70, 1999.

[11] S. LAIZET. *Développement d'un code de calcul combinant des schémas de haute précision avec une méthode de frontière immergée pour la simulation des mouvements tourbillonnaires en aval d'un bord de fuite*. PhD thesis, Université de Poitiers, 2004.

[12] S. LARDEAU. *Simulation numérique directe du contrôle d'écoulements cisaillés libres par injection de fluide*. PhD thesis, Université de Poitiers, 2001.

[13] S. LEE. A numerical study of the unsteady wake behind a sphere in a uniform flow at moderate reynolds numbers. *Computers & Fluids*, 29:639–667, 2000.

[14] C. LINDQUIST. *Contrôle électromagnétique découlements. Études expérimentale et numérique sur le forage découlements initialement au repos et en tunnel hydrodynamique*. PhD thesis, Université Joseph Fourier, 2005.

[15] S. VASUDEVAN T.C. CORKE M.L. POST T.E. McLAUGHLIN M.P. PATEL, T. TERRY and C.F. SUCHOMEL. Scaling effects of an aerodynamic plasma actuator. *AIAA*, 635, 2007.

[16] A.E. PERRY and M.S. CHONG. A description of eddying motions and flow patterns using critical-point concepts. *Annual Review of Fluid Mechanics*, 19:125–155, 1987.

[17] S.K. ROBINSON. Coherent motions in turbulent boundary layers. *Annual Review of Fluid Mechanics*, 23:601–639, 1991.

[18] H. SCHLICHTING. *Boundary-Layer Theory*. McGraw-Hill Series, seventh edition, 1979.

[19] A.G. TOMBOULIDES and S.A. ORSZAG. Numerical investigation of transitional and weak turbulent flow past a sphere. *Journal of Fluid Mechanics*, 416:45–73, 2000.

[20] H. MENG W. YANG and J. SHENG. Dynamics of hairpin vortices generated by a mixing tab in a channel flow. *Experiments in Fluids*, 30:705–722, 2001.

[21] P.G. HUANG Y.B. SUZEN and D.E. ASHPIS. Numerical simulations of flow separation control in low-pressure turbines using plasma actuators. *AIAA*, 937, 2007.